iScience

CellPress
OPEN ACCESS

Article

# Multivalent interactions with RNA drive recruitment and dynamics in biomolecular condensates in *Xenopus* oocytes

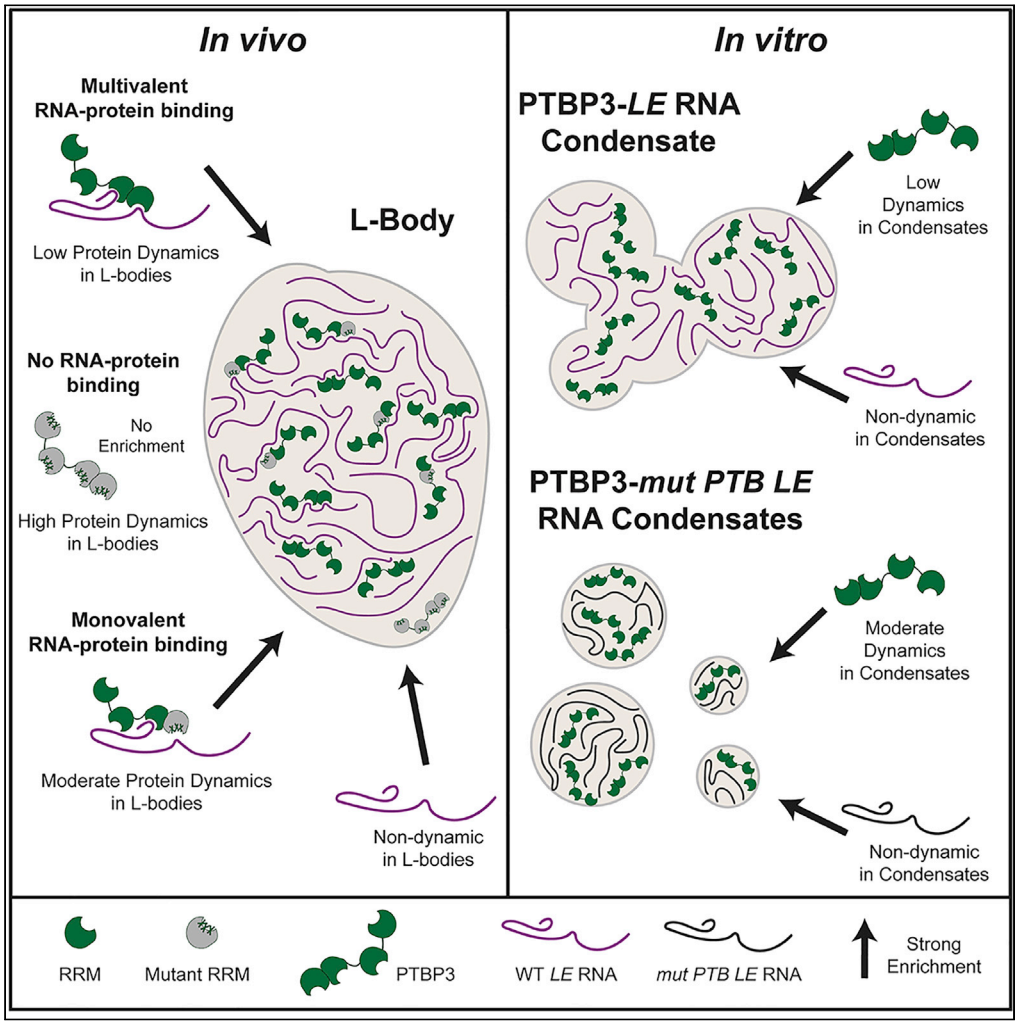


Sarah E. Cabral, Jessica P. Otis, Kimberly L. Mowry

kimberly_mowry@brown.edu

## Highlights

RNA–protein interactions drive recruitment of both RNA and protein to L-bodies

RNA is non-dynamic in both L-bodies and *in vitro* condensates

Multivalent interactions with RNA tune protein dynamics both *in vivo* and *in vitro*

RNA, but not protein, is required for maintenance of the *in vitro* condensates

Cabral et al., iScience *25*, 104811
August 19, 2022 
https://doi.org/10.1016/j.isci.2022.104811

iScience

CellPress
OPEN ACCESS

Article

# Multivalent interactions with RNA drive recruitment and dynamics in biomolecular condensates in *Xenopus* oocytes

Sarah E. Cabral,[1,2] Jessica P. Otis,[1] and Kimberly L. Mowry[1,3,*]

## SUMMARY

**RNA localization and biomolecular condensate formation are key biological strategies for organizing the cytoplasm and generating cellular polarity. In *Xenopus* oocytes, RNAs required for germ layer patterning localize in biomolecular condensates, termed Localization bodies (L-bodies). Here, we have used an L-body RNA-binding protein, PTBP3, to test the role of RNA–protein interactions in regulating the biophysical characteristics of L-bodies *in vivo* and PTBP3–RNA condensates *in vitro*. Our results reveal that RNA–protein interactions drive recruitment of PTBP3 and localized RNA to L-bodies and that multivalent interactions tune the dynamics of the PTBP3 after localization. In a concentration-dependent manner, RNA becomes non-dynamic and interactions with the RNA determine PTBP3 dynamics within these biomolecular condensates *in vivo* and *in vitro*. Importantly, RNA, and not protein, is required for maintenance of the PTBP3–RNA condensates *in vitro*, pointing to a model where RNA serves as a non-dynamic substructure in these condensates.**

## INTRODUCTION

Subcellular compartmentalization is a conserved mechanism by which cells enrich biomolecules for particular processes, allowing for spatial control of biological activity. Many of these compartments, including stress granules, nucleoli, and germ granules, are biomolecular condensates, enriching proteins and RNAs relative to their surroundings without a lipid membrane (reviewed in Boeynaems et al., 2018). The formation of biomolecular condensates is thought to be driven by multivalent interactions, either between "sticker" domains in protein intrinsically disordered regions (IDRs) or between ordered interaction domains, such as multivalent signaling or RNA-binding proteins (RBPs) (reviewed in Mittag and Parker, 2018). These interactions lead to biomolecular condensates with a wide range of biophysical states, with varying dynamics from liquid to gel to solid (reviewed in Alberti et al., 2019). However, the relative contributions of each of these interaction domains to the formation and dynamics of different types of condensates *in vivo* is unclear.

In addition to being enriched for certain types of proteins, a conserved feature of many classes of biomolecular condensates is the incorporation of RNA (reviewed in Fay and Anderson, 2018). Emerging research, particularly *in vitro* studies, suggests that RNA – through both RNA–RNA and RNA–RBP intermolecular interactions – may play a critical role in the structure and assembly of biomolecular condensates (reviewed in Van Treeck and Parker, 2018). However, the role of RNAs and multivalent RBPs in the formation and maintenance of *in vivo* condensates remains unclear and may vary based on the concentration of the RNA and the type of condensate. *In vitro*, low concentrations of RNA often promote liquid-liquid phase separation (LLPS) of proteins (Burke et al., 2015; Lin et al., 2015; Molliex et al., 2015; Patel et al., 2015), whereas high concentrations can inhibit LLPS (Banerjee et al., 2017; Maharana et al., 2018). Conversely, many RNAs are capable of protein-free self-assembly (Jain and Vale, 2017; Langdon et al., 2018; Neil et al., 2021; Van Treeck et al., 2018). *In vivo*, recent studies have shown that RNA may be acting to form a non-dynamic or structural component within a variety of biomolecular condensates (Clemson et al., 2009; Neil et al., 2021; Niepielko et al., 2018; Trcek et al., 2020; Van Treeck et al., 2018).

In *Xenopus* oocytes, translationally silenced RNAs, including *vg1* mRNA, are transported to the vegetal cortex in large cytoplasmic ribonucleoprotein (RNP) granules (reviewed in Cabral and Mowry, 2020). Proper

[1]Department of Molecular Biology, Cell Biology and Biochemistry, Brown University, Providence, RI 02912, USA

[2]Present address: Remix Therapeutics, Cambridge, MA 02139, USA

[3]Lead contact

*Correspondence: kimberly_mowry@brown.edu

https://doi.org/10.1016/j.isci.2022.104811

localization of these RNPs is required for germ layer patterning and mislocalization of vegetally localized mRNAs, such as *vg1*, leads to embryonic lethality (Birsoy et al., 2006; Dale et al., 1993; Thomsen and Melton, 1993). *Cis*-elements within the *vg1* RNA, including polypyrimidine-rich protein binding sites, are required for proper packaging of the RNA into vegetal transport RNPs and localization to the vegetal cortex (Cote et al., 1999; Lewis et al., 2008). Recent work from our laboratory has characterized these RNPs as biomolecular condensates, termed Localization bodies (L-bodies) (Neil et al., 2021). L-bodies are large, irregularly shaped biomolecular condensates that are very highly enriched for localized RNAs. *In vivo*, L-bodies are comprised of a non-dynamic, RNA-containing component enmeshed by a comparatively dynamic protein layer. However, the mechanisms underlying the formation and maintenance of the biophysical state of L-bodies are not known.

Proteomic analysis of L-bodies revealed a strong enrichment for proteins containing RNA binding domains (RBDs), IDRs, or both (Neil et al., 2021), a conserved feature of biomolecular condensates (reviewed in Banani et al., 2017). Many roles have been described for proteins with IDRs in biomolecular condensates, but the functions of ordered, multivalent interaction domains are less well understood. Given the striking non-dynamic state of L-body RNAs, we were particularly interested in characterizing the role of multivalent RBPs in L-body assembly and dynamics. For this, we focused on polypyrimidine tract binding protein 3 (PTBP3), a previously uncharacterized L-body protein that we show in this work to be highly colocalized with L-bodies. PTBP3 is a paralog of the well-characterized RBP, PTBP1 (Yamamoto et al., 1999). In addition to their roles in RNA localization, PTB proteins, such as PTBP1 (hnRNPI), PTBP2 (nPTB), and PTBP3 (ROD1), are involved in many steps in RNA metabolism depending on their subcellular localization and binding partners, including splicing, polyadenylation, mRNA stability, and translation initiation (reviewed in Hu et al., 2018; Sawicka et al., 2008). *In vitro*, PTBP1 phase transitions in the presence of its RNA ligand (Banani et al., 2016; Li et al., 2012). PTB proteins contain four RNA Recognition Motifs (RRMs) that each bind polypyrimidine-rich sequences in RNA (Oberstrass et al., 2005), making PTB an ideal model protein for studying multivalent interactions of well-folded interaction domains within biomolecular condensates.

In this work, we elucidate the role of RNA–RBP interactions in the recruitment and dynamics of components of biomolecular condensates using PTBP3, both *in vivo* and *in vitro*. First, we demonstrate that PTBP3 is an L-body RNA binding protein with moderate *in vivo* mobility and show that PTB–RNA binding is required for the localization and dynamics of both protein and RNA in L-bodies. Next, we show that recombinant PTBP3 phase transitions *in vitro* into non-spherical, solid- or gel-like condensates in an RNA-dependent manner. *In vitro*, as *in vivo*, RNA becomes non-dynamic and PTBP3 dynamics are driven by binding to RNA. Whereas RNA-protein interactions are required for *in vitro* condensate formation, we find that RNA, and not protein, is necessary for condensate maintenance after the degradation of the RNA or protein component, respectively. Finally, we show that a single RNA–RRM interaction is sufficient to target PTBP3 to L-bodies *in vivo*, whereas multivalent interactions between RNA and protein work in concert to tune the mobility of PTBP3 after localization to L-bodies. Taken together, our results indicate that sequence-specific PTBP3–RNA interactions regulate recruitment of both RNA and protein into L-bodies, but that formation of the non-dynamic RNA component is concentration-dependent, rather than sequence-dependent *in vitro*. Moreover, this non-dynamic RNA component is required for condensate maintenance *in vitro*. In L-bodies, it is the strength and number of protein interactions with RNA that drive protein dynamics, suggesting a role for multivalent RNA–RBP interactions in regulating the physical properties of biomolecular condensates.

## RESULTS

### Localization and dynamics of LE RNA in L-bodies require PTB binding sites

Localization of RNAs to L-bodies can be recapitulated by a minimal localization element (*LE* RNA) derived from sequences within the 3′ UTR of the *vg1* mRNA (Cote et al., 1999; Lewis et al., 2004; Neil et al., 2021). *LE* RNA contains two pairs of PTB binding sites and strongly localizes within L-bodies (Figures 1A–1C, S1A, and S1B). This localization is not owing to selective degradation of the RNA, as the microinjected *LE* RNA is stable over 48 h (Figure S1G), and is instead owing to active transport of the RNA (Gagnon et al., 2013; Messitt et al., 2008). To test the role of PTB binding in the localization of RNA to L-bodies, we employed a mutated form of *LE* RNA, termed *mut PTB LE* RNA. The *mut PTB LE* RNA contains three U to A point mutations in each of the four PTB binding sites, but is otherwise identical to the *LE* RNA (Figure S1A), and has been shown to no longer bind to PTBP1 (Lewis et al., 2004). When microinjected into oocytes that contain endogenous *vg1* mRNA, and thus contain L-bodies, *mut PTB LE* RNA is only slightly localized to endogenous L-bodies and, unlike the *LE* RNA, is also observed throughout the oocyte cytoplasm

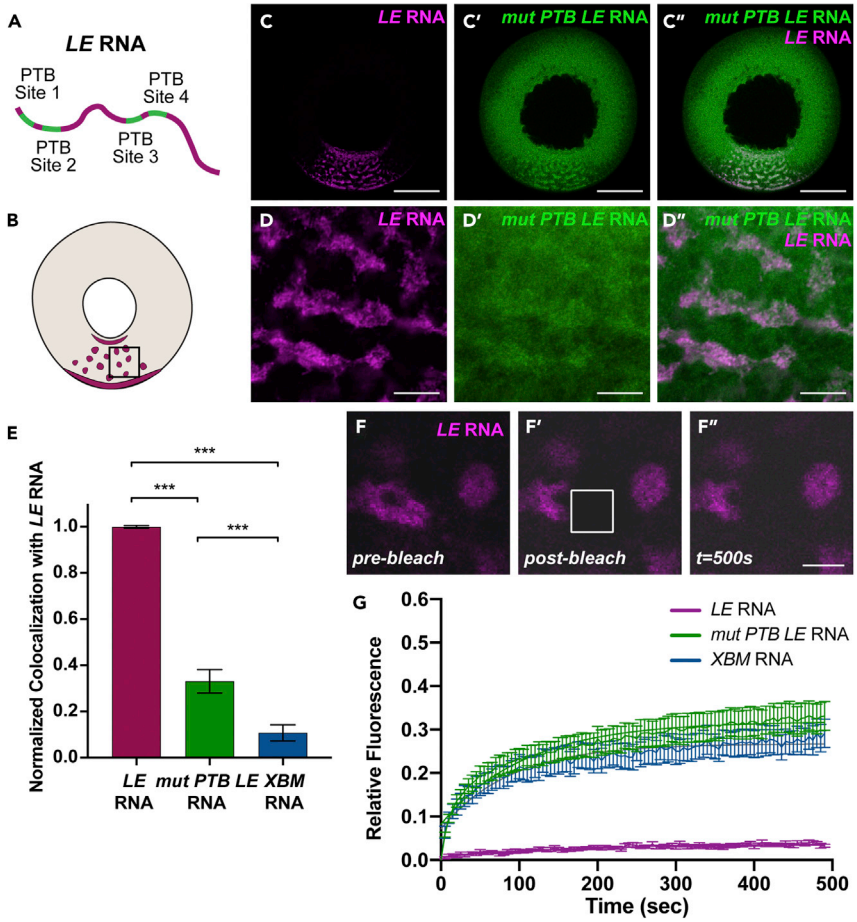


**Figure 1. Localization and dynamics of *LE* RNA in L-bodies requires PTB binding sites**

(A) Schematic of *LE* RNA (magenta) with four polypyrimidine tracts (PTB Sites 1–4) indicated in green.

(B) Schematic of a stage II *Xenopus* oocyte with LE RNA (magenta) localization, as shown in whole oocyte images (as in C); the vegetal cortex is at the bottom. The portion of cytoplasm shown in high magnification images (as in D) is denoted by a black box.

(C) Stage II oocytes were microinjected with fluorescently labeled *LE* RNA (C, magenta) and *mut PTB LE* RNA, with all PTB binding sites mutated, (C′, green). The overlap is shown in C″; scale bars = 100 μm.

(D) High magnification view of L-bodies in a stage II oocyte microinjected with *LE* RNA (D, magenta) and *mut PTB LE* RNA (D′, green). The overlap is shown in D″; scale bars = 10 μm.

(E) Normalized Pearson correlation coefficient of Cy5-labeled *LE* RNA (magenta), *mut PTB LE* RNA (green), and *XBM* RNA (blue) with Cy3-labeled *LE* RNA in stage II oocytes, as in Figures S1A–S1A″, 1C–1C″, and S1C–S1C″. *LE* RNA colocalization with *LE* RNA is set to 1. $n = 30$ oocytes per RNA and error bars represent SEM. *** indicates $p < 0.01$.

(F) An image of the vegetal cytoplasm of an oocyte microinjected with Cy5-labeled *LE* RNA is shown, with a 10 $\mu m^2$ ROI (white); scale bar = 10 μm. F′ and F″ show the post-bleach and 500-s time points, respectively.

(G) Stage II oocytes were microinjected with Cy5-labeled *LE* RNA to mark L-bodies, along with either Cy3-labeled *LE* RNA (magenta), *mut PTB LE* RNA (green), or *XBM* RNA (blue). Normalized FRAP recovery curves are shown. $n = 21$ oocytes and error bars represent SEM. See also Figure S1 and Table S4.

(Figures 1C–1C″). Likewise, as seen at higher magnification, whereas the *LE* RNA is highly localized within L-bodies (Figures 1D, S1C–S1C″), localization of *mut PTB LE* RNA is significantly reduced (Figures 1D′ and 1D″). The *mut PTB LE* RNA is significantly less localized in L-bodies, but is still more colocalized than a non-localizing control, *XBM* RNA, which is neither enriched in nor excluded from L-bodies (Figures 1E, S1D, and S1E). This low, but significant, level of colocalization is likely owing to the binding of *mut PTB LE* RNA to other L-body RBPs, such as Vera, which bind to sites not affected by the *mut PTB LE* RNA mutations (Lewis et al., 2004). Taken together, these data demonstrate that PTB binding to the *LE* RNA is required for robust localization of the RNA into L-bodies.

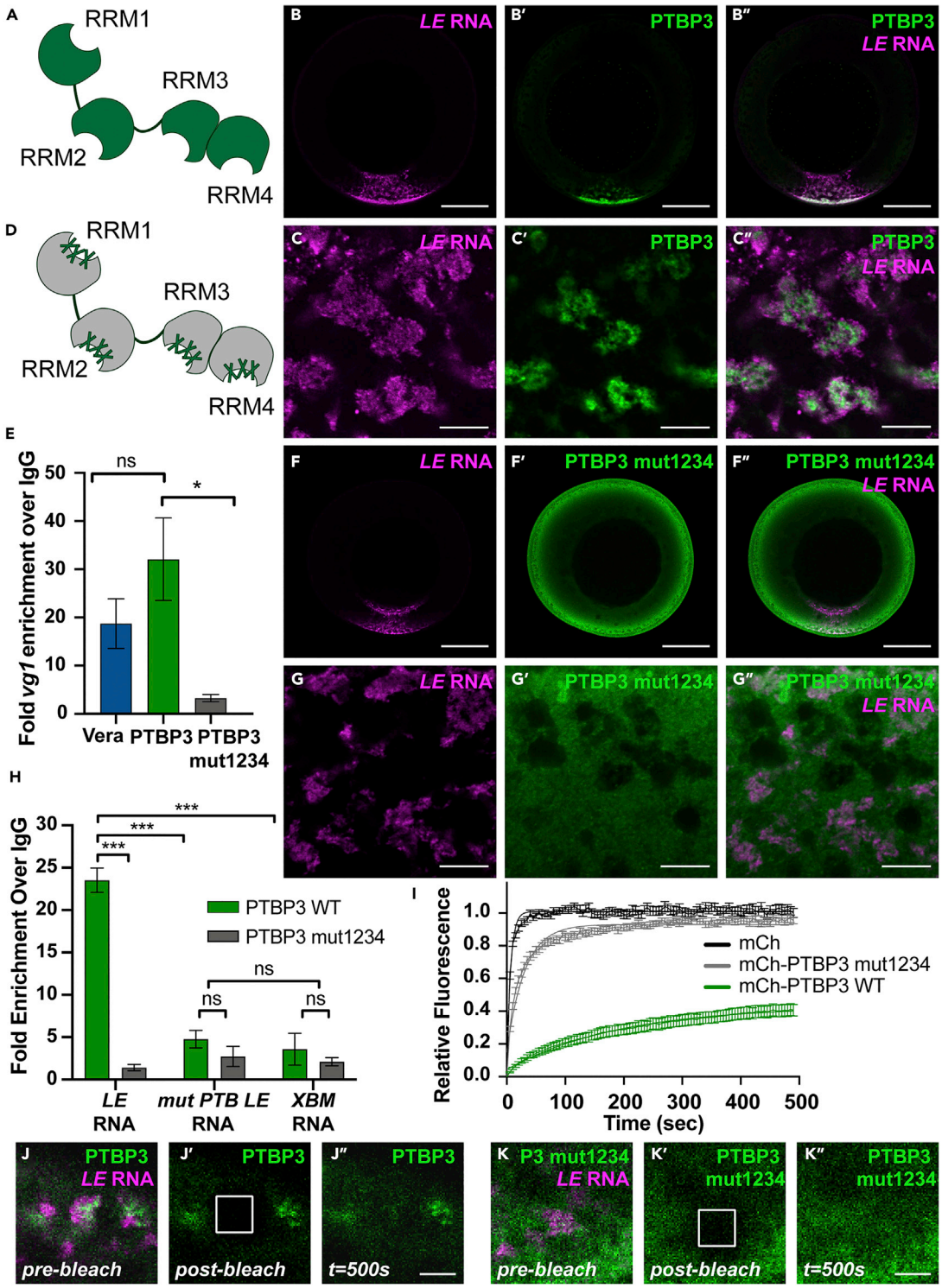


**Figure 2. PTBP3 localization and dynamics in L-bodies require RNA binding**

(A) Schematic of PTBP3 (green) with four RRMs (RRM1-4).

(B) Fluorescently labeled *LE* RNA (B, magenta) was microinjected into stage II oocytes expressing mCh-PTBP3, as detected by anti-mCh IF (B′, green). The overlap is shown in B″; scale bar = 100 μm.

(C) High magnification view of L-bodies in a stage II oocyte microinjected with *LE* RNA (C, magenta) and expressing mCh-PTBP3, as detected by anti-mCh IF (C′, green). The overlap is shown in C″; scale bar = 10 μm.

**Figure 2. *Continued***

(D) Schematic of PTBP3 mut1234 (gray) with three point mutations (green X marks) introduced into each of the four RRMs (Table S1).

(E) Lysates prepared from oocytes expressing Vera-mCh, mCh-PTBP3, or mCh-PTBP3 mut1234 were immunoprecipitated using anti-mCh and IgG. Following the isolation of bound RNAs, *vg1* mRNA was detected via qRT-PCR, with normalization to a *luciferase* extraction control. Shown is fold enrichment for *vg1* mRNA over the IgG control. $n = 3$ and error bars represent SEM. ns indicates $p > 0.5$, * indicates $p < 0.5$. Statistics shown are an Ordinary one-way ANOVA with Tukey's multiple comparison correction.

(F) Fluorescently labeled *LE* RNA (F, magenta) was microinjected into stage II oocytes expressing mCh-PTBP3 mut1234, as detected by anti-mCh IF (F′, green). The overlap is shown in F″; scale bar = 100 μm.

(G) High magnification view of L-bodies in a stage II oocyte microinjected with *LE* RNA (G, magenta) and expressing mCh-PTBP3 mut1234, as detected by anti-mCh IF (G′, green). The overlap is shown in G″; scale bar = 10 μm.

(H) Oocytes expressing mCh-PTBP3 (green) or mCh-PTBP3 mut1234 (gray) were microinjected with *LE*, *mut PTB LE*, and *XBM* RNAs. Oocyte lysates were immunoprecipitated using anti-mCh and IgG. Following the isolation, bound RNAs were detected by qRT-PCR, with normalization to a *luciferase* RNA extraction control. Shown is the fold enrichment for each anti-mCh IP over the IgG control. $n = 3$ and error bars represent SEM. ns indicates $p > 0.5$, *** indicates $p < 0.01$. Statistics shown are an Ordinary one-way ANOVA with Tukey's multiple comparison correction.

(I) Stage II oocytes expressing mCh (black), mCh-PTBP3 (green), or mCh-PTBP3 mut1234 (gray) were microinjected with Cy5-labeled *LE* RNA to mark L-bodies. Normalized FRAP recovery curves are shown. $n = 21$ oocytes and error bars represent the SEM.

(J) An image of the vegetal cytoplasm of an oocyte expressing mCh-PTBP3 and microinjected with Cy5-labeled *LE* RNA to mark L-bodies is shown, with a 10 $\mu m^2$ ROI (white box); scale bar = 10 μm. J′ and J″ show the postbleach and 500-s time points, respectively.

(K) An image of the vegetal cytoplasm of an oocyte expressing mCh-PTBP3mut1234 and microinjected with Cy5-labeled *LE* RNA to mark L-bodies is shown, with a 10 $\mu m^2$ ROI (white box); scale bar = 10 μm. J′ and J″ show the postbleach and 500-s time points, respectively. See also Figures S2, S3 and Tables S1, S4.

As *LE* RNA is known to be non-dynamic in L-bodies (Neil et al., 2021), we next tested the dynamics of the *mut PTB LE* RNA in L-bodies. We microinjected oocytes with Cy3-labeled *LE* RNA, *mut PTB LE* RNA, or *XBM* RNA, along with Cy5-labeled *LE* RNA to mark endogenous L-bodies, and performed fluorescence recovery after photo bleaching (FRAP) on the Cy3-labeled RNAs in L-bodies (Figures 1F and 1G). As expected, *LE* RNA is almost entirely non-dynamic within L-bodies, with an immobile fraction of 93.9% (Figure S1F). By contrast, *mut PTB LE* RNA is significantly more dynamic than the *LE* RNA, with an immobile fraction of 67.7%, and was indistinguishable from *XBM* RNA (72.4% immobile fraction). These results indicate that PTB binding sites are required for both localization of *LE* RNA to L-bodies and the non-dynamic nature of the RNA in L-bodies.

## PTBP3 localization and dynamics in L-bodies require RNA binding

As PTB binding sites in *LE* RNA are necessary for RNA localization, we next tested if RNA binding by PTB is required for protein localization in L-bodies. L-bodies contain two paralogs of PTB, PTBP1 and PTBP3 (Neil et al., 2021). First, we tested the distribution of PTBP1 by expressing mCherry tagged PTBP1 (mCh-PTBP1) in oocytes and assaying the subcellular localization via anti-mCh immunofluorescence (IF) (Figure S2). We found that PTBP1, which shuttles between the nucleus and cytoplasm of *Xenopus* oocytes (Lewis et al., 2008; Xie et al., 2003), is only slightly colocalized with L-bodies in stage II oocytes (Figure S2A), and only becomes significantly colocalized in L-bodies in later stages of oogenesis (Figures S2B and S2C). Interestingly, unlike its paralog PTBP1, mCh-PTBP3 was not detected in the nucleus and is highly localized to L-bodies, when they are first evident in stage II of oogenesis (Figure 2B). Therefore, we focused on PTBP3 for our experiments.

PTBP3 is an RNA-binding protein containing four well-folded RNA recognition motifs (RRMs; Figure 2A). The PTBP3 RRMs bind to polypyrimidine tracts in RNA, here termed PTB sites (Yamamoto et al., 1999). To determine the distribution of PTBP3 in oocytes, we expressed mCherry-tagged PTBP3 (mCh-PTBP3) in stage II-III oocytes and assayed the subcellular localization using anti-mCh IF. At low magnification, mCh-PTBP3 is highly restricted to the vegetal cytoplasm of oocytes, particularly at the vegetal cortex and in the lower vegetal cytoplasm and is colocalized with *LE* RNA (Figures 2B–2B″). At higher magnification, mCh-PTBP3 is observed to be highly localized to L-bodies (Figures 2C–2C″). As PTBP3 is highly colocalized within L-bodies *in vivo*, PTB binding sites are required for *LE* RNA localization, and it has a clear, multivalent RBD domain structure, we used PTBP3 as a model protein to probe the role of RNA binding in the localization of proteins to L-bodies and their dynamics after localization.

To determine whether RNA-binding is required for the localization of mCh-PTBP3 to L-bodies, point mutations analogous to those that have been demonstrated to disrupt RNA-binding in human PTBP1 (Kafasla et al., 2011) were introduced into *Xenopus* PTBP3 (Figure 2D and Table S1). Three specific point mutations were engineered into each of the four mCh-PTBP3 RRMs to create a quadruple RRM mutant (mCh-PTBP3 mut1234), which expresses in oocytes containing endogenous wild type PTBP3 at comparable levels to the

mCh-PTBP3 (Figure S3). First, to test whether the RRM mutations affected the interaction between PTBP3 and *vg1* RNA, we expressed mCh-PTBP3 or mCh-PTBP3 mut1234 in oocytes and performed RNA immunoprecipitation (RIP) experiments using Vera-mCh, a well-established *vg1* mRNA binding protein as a positive control (Lewis et al., 2004) (Figure 2E). mCh-PTBP3 immunoprecipitated endogenous *vg1* mRNA comparably to Vera-mCh, showing that PTBP3 interacts with *vg1* mRNA in oocytes. Conversely, immunoprecipitation of *vg1* mRNA was significantly decreased in the mCh-PTBP3 mut1234 injected oocytes, demonstrating that the mutations inserted into PTBP3 significantly reduce binding to endogenous *vg1* mRNA *in vivo*. In addition to the RNA-binding deficiency, we cannot exclude the possibility that the mutations inserted into PTBP3 also disrupt some protein–protein interactions either directly or through RNA-binding-dependent interactions.

We also used RIP experiments to determine whether the mutation of the PTB binding sites in *mut PTB LE* RNA blocked binding to PTBP3. Oocytes were microinjected with either mCh-PTBP3 or mCh-PTBP3 mut1234, along with *LE* RNA, *mut PTB LE* RNA, and *XBM* RNA. Following immunoprecipitation with anti-mCh and IgG as a negative control, the fold enrichment of each RNA was assayed via RT-qPCR (Figure 2H). As with the endogenous *vg1* mRNA, mCh-PTBP3 strongly immunoprecipitated the *LE* RNA, whereas the mCh-PTBP3 mut1234 did not; further demonstrating that the PTBP3 RRM mutations disrupt RNA binding. Importantly, neither mCh-PTBP3 nor mCh-PTBP3 mut1234 immunoprecipitated the *mut PTB LE* or *XBM* RNAs significantly over IgG controls. We conclude from these results that PTBP3 binds to one or more of the PTB binding sites in the *LE* RNA.

To determine whether the binding of PTBP3 to RNA is required for localization of PTBP3 to L-bodies, we tested the subcellular distribution of mCh-PTBP3 mut1234 in stage II-III oocytes containing wild-type endogenous PTBP3 and thus forming L-bodies. In contrast to wild-type mCh-PTBP3 (Figures 2B–2B″), mCh-PTBP3 mut1234 is distributed throughout the oocyte cytoplasm, and is not colocalized with *LE* RNA in L-bodies (Figures 2F–2F″). At high magnification, mCh-PTBP3 mut1234 is neither enriched nor excluded from L-bodies, but is nearly ubiquitous in the vegetal cytoplasm (Figures 2G–2G″), in marked contrast to wild-type PTBP3 (Figures 2C–2C″). These results indicate that the mutations inserted into PTBP3 mut1234 that block RNA binding also disrupt localization to L-bodies.

Our previous work suggested a model for an L-body structure in which localizing RNAs form a non-dynamic component, enmeshed by proteins exhibiting a range of moderate to high mobilities (Neil et al., 2021). Here, we hypothesize that the dynamics of L-body proteins are regulated by direct binding to RNA. Thus, PTBP3, which binds *vg1* mRNA (Figure 2E), should be moderately dynamic within L-bodies, whereas the quadruple RRM mutant should be significantly more dynamic. To test this hypothesis, we expressed mCh, mCh-PTBP3, or mCh-PTBP3 mut1234 in stage II oocytes and analyzed the protein dynamics *in vivo* using FRAP (Figures 2I–2K). As predicted, mCh-PTBP3 is moderately dynamic, with an immobile fraction of 52.4%, whereas mCh-PTBP3 mut1234 was significantly more dynamic, with an immobile fraction of 6.3%, and more closely resembled the mCh alone control. Taken together, these data indicate that the binding of PTBP3 to RNA is necessary for its localization to L-bodies, and that binding to non-dynamic L-body RNA(s) regulates the dynamics of the protein within L-bodies.

### Recombinant PTBP3 and LE RNA phase transition into solid or gel-like condensates *in vitro*

To probe the potential role of interactions between PTBP3 and RNA in phase transitions, we developed an *in vitro* assay using recombinant PTBP3, purified under high salt conditions to minimize co-purification of contaminating nucleic acids (Figures S4A and S4B) and *in vitro* transcribed *LE* RNA. Purified PTBP3 was mixed with *LE* RNA and incubated at room temperature for 1 h without a crowding agent. To quantify the degree of phase transitions across different conditions, turbidity was assayed (Sanulli and Narlikar, 2021). First, to assess the role of electrostatic interactions on phase transitions, the turbidity of PTBP3 and *LE* RNA or PTBP3 alone was tested across increasing salt concentrations (Figure 3A). Across all NaCl concentrations tested, no significant turbidity was detected with PTBP3 alone, indicating that RNA is required for phase transition *in vitro*. However, with PTBP3 and *LE* RNA, turbidity was detected in a salt-dependent manner; maximum phase transition was observed at intermediate levels of NaCl, but was inhibited at both low and high concentrations. Next, to assess the role of RNA on phase transitions, the turbidity of PTBP3 and *LE* RNA or *LE* RNA alone was tested across an RNA concentration series (Figure 3B). No turbidity was observed with *LE* RNA alone even at the highest concentrations tested, indicating that the observed phase transition requires PTBP3 and is not due solely to RNA–RNA interactions. With both PTBP3 and *LE* RNA, phase transition was detected in an RNA-dependent manner,

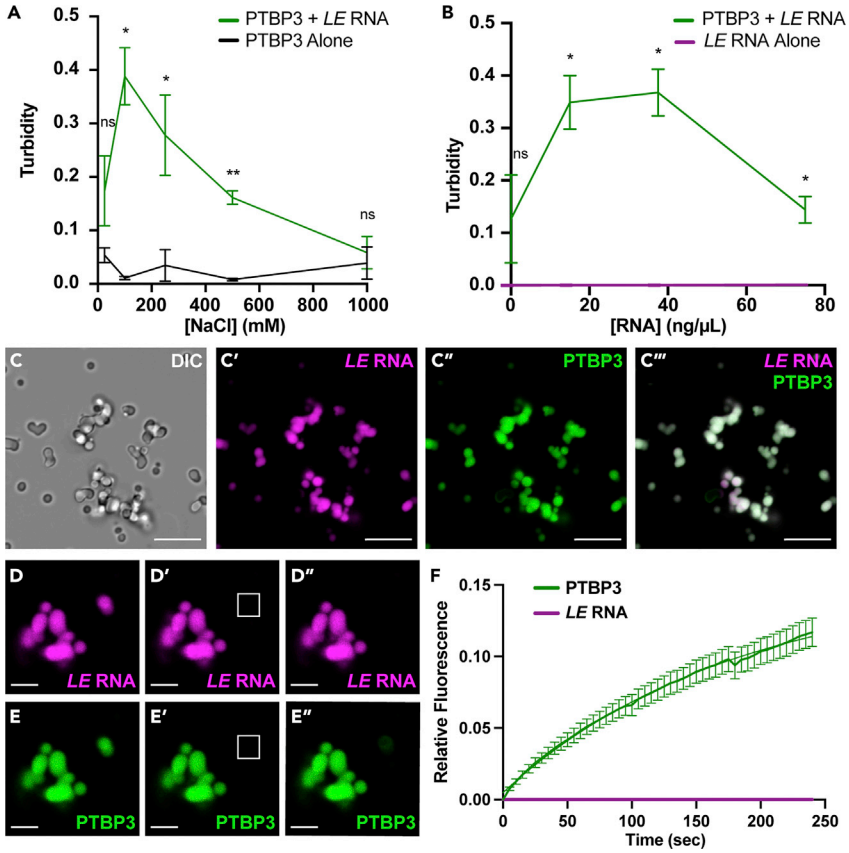


**Figure 3. Recombinant PTBP3 and *LE* RNA phase transition into solid or gel-like condensates *in vitro***

(A) PTBP3 and *LE* RNA together (green) or PTBP3 alone (black) were incubated in the indicated concentrations of NaCl for 1 h at room temperature. Phase transitions were monitored by turbidity, measured by OD600. Error bars represent the SEM $n = 3$. ns indicates $p > 0.5$, * indicates $p < 0.5$, ** indicates $p < 0.1$.

(B) PTBP3 and *LE* RNA together (green) or *LE* RNA alone (magenta) were incubated in the indicated concentrations of *LE* RNA for 1 h at room temperature. Phase transitions were monitored by turbidity, measured by OD600. Error bars represent the SEM $n = 3$. ns indicates $p > 0.5$, * indicates $p < 0.5$. Statistics shown are multiple paired t tests using a two-stage step-up method.

(C) 12.5-μM AF647-labeled PTBP3 was incubated with 15 ng/μL AF488-labeled *LE* RNA for 1 h at room temperature. The resulting condensates are shown by DIC (C), and fluorescent imaging for *LE* RNA (C′, magenta) and PTBP3 (C″, green). The overlay is shown in C‴; scale bars = 10 μm.

(D–E) An image of PTBP3-*LE* condensates is shown with a 2 $\mu m^2$ FRAP ROI (white).

(D) *LE* RNA fluorescence pre-bleach, postbleach (D′), and 4 min post-recovery (D″). Scale bars = 2 μm.

(E) AF647-PTBP3 fluorescence pre-bleach, post-bleach (E′), and 4 min post-recovery (E″).

(F) Normalized FRAP recovery curves are shown for PTBP3-*LE* RNA condensates, carried out as in D–E. $n = 21$ condensates per RNA and error bars represent SEM. See also Figure S4 and Table S4.

indicating that RNA is required for phase transitions. Importantly, phase transition was inhibited by high concentrations of *LE* RNA, indicating that multivalent interactions between PTBP3 and *LE* RNA may be important for *in vitro* condensate formation.

To further analyze *in vitro* phase transition of PTBP3 and *LE* RNA, condensates formed at intermediate salt and RNA concentrations were visualized by microscopy. When incubated together, PTBP3 and *LE* RNA formed non-spherical structures that were highly enriched for both the protein and RNA components (Figures 3C–3C‴). Whereas some condensates appeared round, as would be expected for liquid condensates owing to surface tension (Hyman et al., 2014), other condensates appeared to be comprised of multiple small droplets that had interacted to form larger structures, but not fused and reformed into a larger sphere. Under these conditions, neither PTBP3 nor *LE* RNA formed condensates alone (Figures S4D and S4E), supporting a critical role for protein-RNA interactions in the phase transition. To characterize the

dynamics of the protein and RNA in the *in vitro* condensates, we performed FRAP. *LE* RNA (Figures 3D–3D″) was non-dynamic *in vitro* (immobile fraction = 99.8%), indicating that in *in vitro* condensates, *LE* RNA forms a solid or gel-like component (Figures 3F and S4C). PTBP3 (Figures 3E–3E″), whereas significantly more dynamic than *LE* RNA, was only moderately dynamic within the *in vitro* condensates (immobile fraction = 82.0%) (Figures 3F and S4C). These results demonstrate that interactions between *LE* RNA and PTBP3 are sufficient to drive phase transition into non-spherical condensates *in vitro,* with trends in RNA and protein dynamics mirroring the findings in *in vivo* L-bodies: both *in vivo* and *in vitro, LE* RNA is non-dynamic and PTBP3 is significantly more dynamic than the RNA.

### Maintenance of *PTBP3 and* LE *RNA condensates* requires RNA, but not the protein component

Whereas PTBP3-*LE* RNA *in vitro* condensate formation requires both protein and RNA, the components required for the maintenance of the condensates were not known. To test this, we formed *in vitro* condensates under the same conditions as above, followed by treatment with DNase, RNase, or Proteinase K (Figure 4). With DNase treatment, no significant change was observed in the fluorescence of PTBP3 or *LE* RNA (Figures 4A and 4B, Video S1). With RNase treatment, however, both the *LE* RNA and PTBP3 fluorescence decreased rapidly, suggesting that the RNA, facilitating either RNA–RNA or RNA–protein interactions, is required for the maintenance of the condensates (Figures 4C and 4D, Video S2). Conversely, with Proteinase K treatment, whereas the PTBP3 fluorescence decreased rapidly, the *LE* RNA fluorescence was substantially resistant to degradation of the protein component and remained in the condensates for several minutes after protein degradation was complete (Figures 4E and 4F, Video S3). Importantly, these results were not owing to incomplete proteolysis as no large molecular weight products were observed after Proteinase K treatment (Figure S5). Taken together, these results suggest that, whereas RNA–protein interactions are required for *in vitro* condensate formation, RNA–RNA interactions are sufficient to maintain the RNA within the condensates following degradation of the protein.

### In vitro condensate morphology and PTBP3 dynamics are dependent on RNA-binding

To test whether the phase transition of PTBP3 *in vitro* is dependent on specific RNA sequences, we compared the phase transition of PTBP3 in the presence of *mut PTB LE* RNA, *XBM* RNA, and *LE* RNA, as above. For each of the RNAs, PTBP3 formed condensates that incorporated both PTBP3 and the RNA (Figures 5A–5C), demonstrating that although *in vitro* condensate formation requires RNA, it does not require the interaction of PTBP3 specifically with PTB sites that are present only in *LE* RNA. For *in vitro* condensates, unlike *in vivo* L-bodies, there was no difference in partitioning of *LE* RNA, *mut PTB LE* RNA, or *XBM* RNA into PTBP3 condensates (Figure S6B). However, the morphologies of the *in vitro* condensates formed by PTBP3 with *LE* RNA, *mut PTB LE* RNA, and *XBM* RNA are distinct from one another (Figures S6C–S6E). PTBP3 and *LE* RNA (Figures 5A, S6C–S6E) formed fewer, larger, and more irregularly shaped structures, whereas condensates formed with PTBP3 and *XBM* RNA were smaller, more numerous, and significantly more circular (Figures 5C, S6C–S6E). Condensates formed *in vitro* with PTBP3 and *mut PTB LE* RNA displayed an intermediate morphology, but more closely resembled *XBM* RNA condensates (Figures 5B, S6C–S6E). Importantly, none of these differences were owing to differences in RNA size as all *in vitro* transcribed RNAs were precisely length matched.

The differences in *in vitro* condensate morphology led us to hypothesize that these different types of condensates may have varying protein and/or RNA dynamics. To test this, we performed FRAP on the protein and RNA in each type of *in vitro* condensate. Surprisingly, each of the RNAs was non-dynamic, exhibiting mobilities that are not significantly different from one another (Figure 5D), with immobile fractions for whole condensate FRAP of 99.8%, 99.7%, and 99.5% for the *LE, mut PTB LE,* and *XBM* RNA, respectively. Similarly, all RNAs were also non-dynamic via partial condensate FRAP (Figure S7). These data suggest that *in vitro*, as in L-bodies *in vivo*, RNA is non-dynamic. However, unlike *in vivo*, RNA is non-dynamic *in vitro* regardless of the primary sequence of the RNA. Conversely, dynamics of PTBP3 protein were dependent on the sequence of the RNA incorporated into the *in vitro* condensates; PTBP3 was the least mobile in condensates formed with *LE* RNA (immobile fraction = 82.0%), and significantly more mobile in condensates formed with *mut PTB LE* (immobile fraction = 71.5%) or *XBM* RNA (immobile fraction = 64.8%) (Figures 5E and S6A). These data suggest that PTBP3 dynamics *in vitro* are dependent on the ability to interact with the non-dynamic RNA, consistent with our *in vivo* results. When treated with DNase, RNase, or protease, the PTBP3-*mut PTB LE* and PTBP3-*XBM in vitro* condensates responded similarly to the PTBP3-*LE* condensates: no change was observed with DNase treatment, both protein and RNA were concurrently released

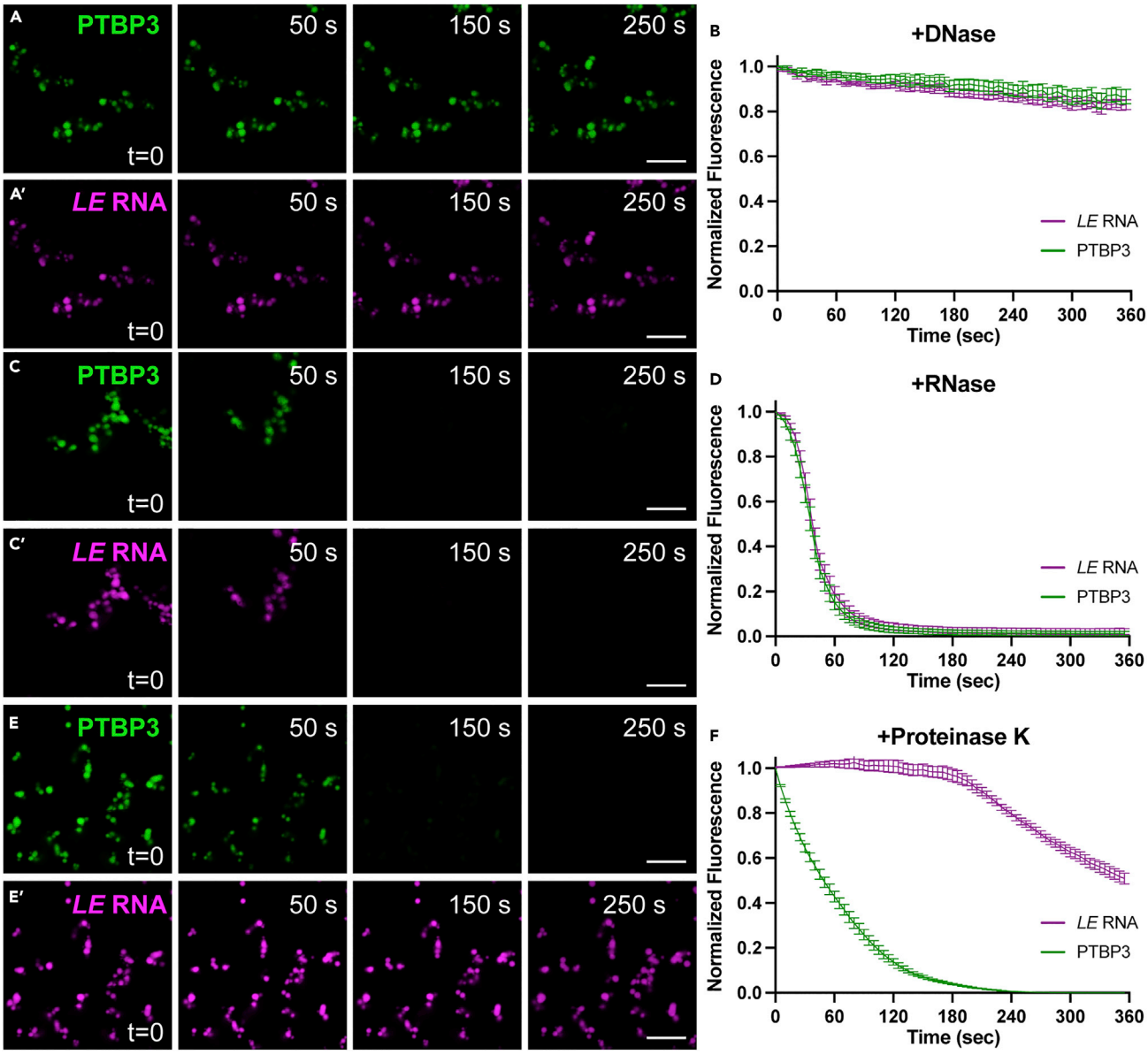


**Figure 4. Maintenance of PTBP3 and *LE* RNA condensates requires RNA, but not protein**

(A) 12.5-μM AF647-labeled PTBP3 was incubated with 15 ng/μL AF488-labeled *LE* RNA for 1 h at room temperature and then treated with 0.18 U/μL DNase. Shown is representative fluorescent imaging for *LE* RNA (A, magenta) and PTBP3 (A′, green) immediately after enzyme addition ($t$ = 0), after 50, 150, and 250 s; scale bars = 10 μm. See Video S1.

(B) Fluorescence over time relative to $t$ = 0 s is shown for *LE* RNA (magenta) and PTBP3 (green) following DNase treatment. Fluorescence over time was analyzed for 50 × 50 ROIs ($n$ = 10) from three replicates; error bars show the SEM.

(C) 12.5-μM AF647-labeled PTBP3 was incubated with 15 ng/μL AF488-labeled *LE* RNA for 1 h at room temperature and then treated with 0.05 U/μL RNase A and 1.82 U/μL RNase T1. Shown is representative fluorescent imaging for *LE* RNA (C, magenta) and PTBP3 (C′, green) immediately after enzyme addition ($t$ = 0), after 50, 150, and 250 s; scale bars = 10 μm. See Video S2.

(D) Fluorescence over time relative to $t$ = 0 s is shown for *LE* RNA (magenta) and PTBP3 (green) following RNase treatment. Fluorescence over time was analyzed for 50 × 50 ROIs ($n$ = 10) from three replicates; error bars show the SEM.

(E) 12.5-μM AF647-labeled PTBP3 was incubated with 15 ng/μL AF488-labeled *LE* RNA for 1 h at room temperature and then treated with 1.14 mg/mL Proteinase K. Shown is representative fluorescent imaging for *LE* RNA (E, magenta) and PTBP3 (E′, green) immediately after enzyme addition ($t$ = 0), after 50, 150, and 250 s; scale bars = 10 μm. See Video S3.

(F) Fluorescence over time relative to $t$ = 0 s is shown for *LE* RNA (magenta) and PTBP3 (green) following Proteinase K treatment. Fluorescence over time was analyzed for 50 × 50 ROIs ($n$ = 10) from three replicates; error bars show SEM. See also Figure S5.

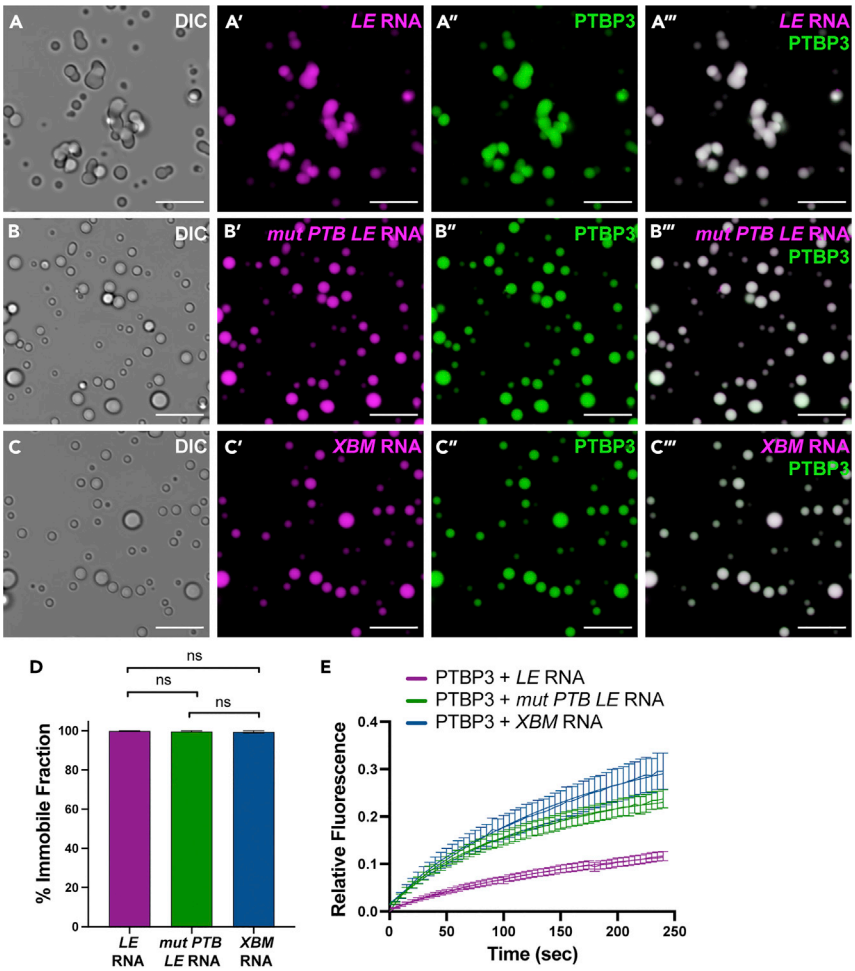


**Figure 5. *In vitro* condensate morphology and PTBP3 dynamics are dependent on RNA-binding**

(A) 12.5-μM AF647-labeled PTBP3 was incubated with 15 ng/μL AF488-labeled *LE* RNA for 1 h at room temperature. The resulting condensates are shown in DIC (A), and by fluorescence imaging for *LE* RNA (A′, magenta), and PTBP3 (A″, green). The overlay is shown in A‴; scale bars = 10 μm.

(B) 12.5-μM AF647-labeled PTBP3 was incubated with 15 ng/μL AF488-labeled *mut PTB LE* RNA for 1 h at room temperature. The resulting condensates are shown in DIC (B), and by fluorescence imaging for *mut PTB LE* RNA (B′, magenta), and PTBP3 (B″, green). The overlay is shown in B‴; scale bars = 10 μm.

(C) 12.5-μM AF647-labeled PTBP3 was incubated with 15 ng/μL AF488-labeled *XBM* RNA for 1 h at room temperature. The resulting condensates are shown in DIC (C), and by fluorescence imaging for *XBM* RNA (C′, magenta), and PTBP3 (C″, green). The overlay is shown in C‴; scale bar = 10 μm.

(D) % immobile fraction for RNA FRAP of *in vitro* condensates. Error bars represent the SEM. ns indicates $p > 0.5$.

(E) Normalized FRAP recovery curves for are shown for PTBP3 in condensates containing PTBP3-*LE* RNA (magenta), PTBP3-*mut PTB LE* RNA (green), and PTBP3-*XBM* RNA (blue). $n = 21$ condensates per RNA and error bars represent SEM.

See also Figures S6, S7, S8 and Table S4.

from the condensates with RNase treatment, and RNA was partially resistant to loss of the protein with protease treatment (Figures S8 and S9).

## PTBP3 dynamics in L-bodies are dependent on multivalent interactions with RNA

Because PTBP3 dynamics depend on interaction with RNA both *in vivo* and *in vitro*, we next asked whether this relies on specific PTBP3 RRMs or combinations of PTBP3 RRMs. To test the role of multivalency, we took an *in vivo* approach as recombinant PTBP3 RRM mutants exhibited poor solubility *in vitro*, particularly after cleavage of the maltose binding protein (MBP) tag. However, *in vivo*, the expression and solubility of the mutant PTBP3 proteins in oocytes were comparable to that of WT PTBP3 (Figure S3). First, we engineered PTBP3

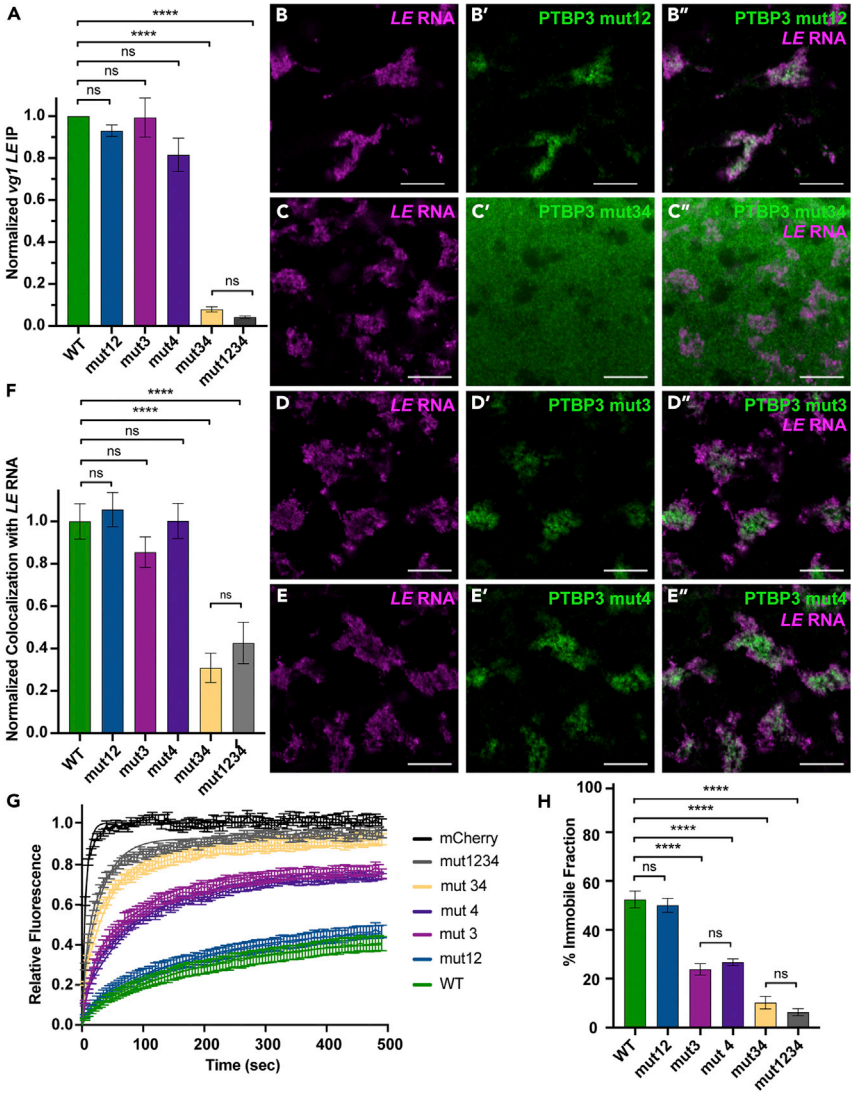


**Figure 6. PTBP3 dynamics in L-bodies are dependent on multivalent interactions with RNA**

(A) Oocytes expressing mCh-PTBP3 (green), mCh-PTBP3 mut12 (blue), mCh-PTBP3 mut34 (yellow), mCh-PTBP3 mut3 (magenta), mCh-PTBP3 mut4 (purple), and mCh-PTBP3 mut1234 (gray) were microinjected with *LE* RNA. Oocyte lysates were immunoprecipitated using anti-mCh and IgG. Following the isolation of bound RNAs, *LE* RNA was detected via qRT-PCR, with normalization to a luciferase RNA extraction control. Fold enrichment for mCh-PTBP3 WT over the IgG control is set to 1. $n = 3$ and error bars represent the SEM. ns indicates $p > 0.5$, **** indicates $p < 0.001$. Statistics shown are an Ordinary one-way ANOVA with Tukey's multiple comparison correction.

(B) High magnification view of L-bodies in a stage II oocyte microinjected with LE RNA (B, magenta) and expressing mCh-PTBP3 mut12, as detected by anti-mCh IF (B′, green). The overlap is shown in B″; scale bars = 10 μm.

(C) High magnification view of L-bodies in a stage II oocyte microinjected with *LE* RNA (C, magenta) and expressing mCh-PTBP3 mut34, as detected by anti-mCh IF (C′, green). The overlap is shown in C″; scale bars = 10 μm.

(D) High magnification view of L-bodies in a stage II oocyte microinjected with *LE* RNA (D, magenta) and expressing mCh-PTBP3 mut3, as detected by anti-mCh IF (D′, green). The overlap is shown in D″; scale bars = 10 μm.

(E) High magnification view of L-bodies in a stage II oocyte microinjected with *LE* RNA (E, magenta) and expressing mCh-PTBP3 mut4, as detected by anti-mCh IF (E′, green). The overlap is shown in E″; scale bars = 10 μm.

(F) Normalized Pearson correlation coefficient of mCh-PTBP3 WT (green), mCh-PTBP3 mut12 (blue), mCh-PTBP3 mut34 (yellow), mCh-PTBP3 mut3 (magenta), mCh-PTBP3 mut4 (purple), and mCh-PTBP3 mut1234 (gray) with *LE* RNA in stage II oocytes. mCh-PTBP3 WT colocalization with *LE* RNA is set to 1. $n = 30$ oocytes per protein and error bars represent SEM. ns indicates $p > 0.5$, **** indicates $p < 0.001$.

**Figure 6. *Continued***

(G) Stage II oocytes expressing mCh-PTBP3 WT (green), mCh-PTBP3 mut12 (blue), mCh-PTBP3 mut34 (yellow), mCh-PTBP3 mut3 (magenta), mCh-PTBP3 mut4 (purple), and mCh-PTBP3 mut1234 (gray) were microinjected with Cy5-labeled *LE* RNA to mark L-bodies. Normalized FRAP recovery curves are shown. $n = 21$ oocytes per protein and error bars represent the SEM.

(H) % immobile fraction for protein FRAP experiments shown in (G). Error bars represent the SEM. ns indicates $p > 0.5$, **** indicates $p < 0.001$. See also Figure S3 and Tables S1, S4.

double RRM mutants (mut12 and mut34), expressed them in stage II oocytes, and tested the double RRM mutants for their ability to bind *LE* RNA *in vivo* by RIP (Figure 6A). mCh-PTBP3 mut12 immunoprecipitated *LE* RNA comparably to the wild-type protein, suggesting that RRMs one and two are not required for binding *LE* RNA *in vivo*. By contrast, mCh-PTBP3 mut34 immunoprecipitated *LE* RNA comparably to mCh-PTBP3 mut1234, suggesting that RRM3, RRM4, or both RRMs are required for binding to *LE* RNA. To distinguish between these possibilities, we created single RRM mutants (mut3 and mut4) and tested their ability to immunoprecipitate *LE* RNA. Both mCh-PTBP3 mut3 and mCh-PTBP3 mut4 immunoprecipitated *LE* RNA comparably to the wild-type and mCh-PTBP3 mut12 proteins, demonstrating that *LE* RNA can bind to RRM3 and RRM4. Hence, intact forms of RRM3 or RRM4 are both necessary and sufficient for robust *LE* RNA binding *in vivo*.

To test whether specific PTBP3 RRMs drive localization to L-bodies, we expressed each of the double and single PTBP3 RRM mutants *in vivo* and assayed their subcellular distribution using mCh IF. We found that *LE* RNA binding by PTBP3 RRM mutants predicts localization to L-bodies: mCh-PTBP3 mut12 is colocalized with L-bodies (Figures 6B–6B″, 6F), whereas mCh-PTBP3 mut34 showed no colocalization (Figures 6C–6C″, 6F); mCh-PTBP3 mut3 and mCh-PTBP3 mut4 single RRM mutants strongly colocalize with L-bodies (Figures 6D–6D″, 6E–6E″, 6F). These results show that binding to RNA by either RRM3, RRM4, or RRM3 and 4 is sufficient to drive the localization of PTBP3 in L-bodies and that this localization does not require multivalent interactions between protein and RNA.

Whereas RNA binding by a single RRM is sufficient to drive protein localization, we reasoned that interaction between the non-dynamic RNA and multiple RRMs may be required for the moderate dynamics of the wild-type PTBP3 protein in L-bodies. To test the role of multivalent interactions in protein dynamics, we tested each of the PTBP3 mutants by FRAP (Figures 6G and 6H). The dynamics of mCh-PTBP mut12 (immobile fraction = 50.1%), was indistinguishable from the wild-type protein, and mCh-PTBP3 mut34 (immobile fraction = 10.2%) was indistinguishable from mCh-PTBP3 mut1234, as in the RIP and colocalization experiments. However, as predicted by our model, mCh-PTBP3 mut3 and mCh-PTBP3 mut four showed intermediate dynamics with immobile fractions of 23.9 and 26.7%, respectively, and were indistinguishable from one another. These results demonstrate that RNA–PTBP3 binding to a single RRM is sufficient for localization to L-bodies, whereas multivalent interactions with RNA act in combination to regulate the dynamics of the protein within L-bodies.

## DISCUSSION

### Proposed model for L-body component recruitment and dynamics

In this work, we have dissected the role of RBP–RNA binding in L-bodies using both *in vivo* and *in vitro* techniques. L-bodies are recently identified, irregularly shaped biomolecular condensates with a non-dynamic RNA component and a comparatively dynamic protein component (Neil et al., 2021). However, the mechanisms underlying the range of biophysical states observed in L-body components were unclear. Here, we propose a multistep model for L-body component recruitment and dynamics based on both specific RNA–RBP binding and RNA concentration-dependent effects using the protein PTBP3 as a model (Figure 7). Whereas PTBP3 binding is a central player in *LE* RNA localization, many other L-body RBPs may follow similar patterns of RNA-binding dependent dynamics within the oocyte.

First, RBPs bind localizing RNAs in the oocyte cytoplasm, driving the localization of the RBP and RNA within L-bodies. Accordingly, PTBP3 strongly colocalizes with L-bodies, but PTBP3 mut1234, which no longer binds to the *LE* RNA, is nearly ubiquitous throughout the cytoplasm. Similarly, *LE* RNA localization is a defining feature of L-bodies, but *mut PTB LE* and *XBM* RNAs, which do not bind to PTB, are both distributed throughout the cytoplasm. Therefore, sequence-specific RNA–protein binding is required for both the RNA and the RBP to localize to L-bodies in *Xenopus* oocytes. These results point to PTBP3 as a novel regulator of L-body RNA incorporation, adding mechanistic insight into the compositional control of condensates that are required to pattern the developing embryo. Unfortunately, direct depletion of the endogenous PTBP3 protein to assess its role in *LE* RNA localization to L-bodies was not possible within

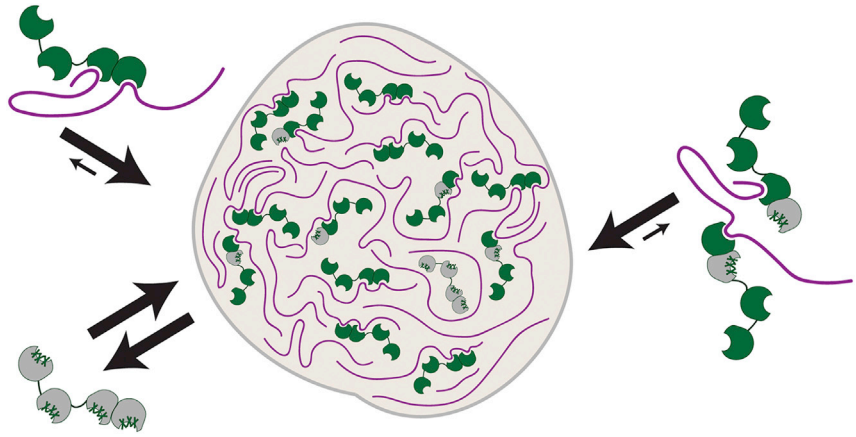

**Figure 7. Model for recruitment and dynamics of PTBP3 and localized RNAs in L-bodies**

RBPs, such as PTBP3 (green), bind localizing RNAs (magenta) in a sequence-dependent manner that is required for both RNA and protein localization to L-bodies (tan), such that PTBP3 RNA-binding mutants (gray) are neither enriched nor excluded from L-bodies. Once localized, locally high concentrations cause RNAs to become solid or gel-like in a sequence-independent manner within the L-body. Arrows denote movement of proteins or RNAs into and out of the L-body, with the arrow thickness indicating the relative amount of this movement. RNA-protein interaction with one RRM is sufficient to target PTBP3 to L-bodies, whereas the strength of number of interactions with non-dynamic RNA tunes the protein dynamics within the L-body such that PTBP3 with a single RNA-binding RRM is more dynamic than PTBP3 with two RNA-binding RRMs.

this *in vivo* system. The *in vitro* RNA–PTBP3 condensates, however, enrich equally for all RNAs as this step of regulation is not present in the minimal *in vitro* system. Instead, non-specific interactions between PTBP3 and *mut PTB LE* or *XBM* RNA are sufficient to drive phase transition *in vitro*.

Next, following RBP and RNA localization, locally high concentrations of RNA within the L-body facilitate intermolecular RNA–RNA interactions, leading the RNA to exhibit solid or gel-like dynamics. *In vivo*, *LE* RNA, which is highly concentrated within the L-body, is almost entirely non-dynamic, whereas *mut PTB LE* and *XBM* RNAs are not enriched within L-bodies and are much more dynamic. These dynamics are not a property of RNA size, as *LE, mut PTB LE,* and *XBM* RNAs are precisely length-matched, and previous work has demonstrated that RNA mobility in *in vivo* L-bodies also does not correlate with RNA length (Neil et al., 2021). Whereas the *in vivo* data do not distinguish between differences in RNA dynamics owing to a lack of PTBP3 binding and RNA concentration-dependent effects, the *in vitro* data suggests that the process may be RNA concentration dependent; RNA gelation occurs in the *in vitro* PTBP3–RNA condensates, driving *LE, mut PTB LE,* and *XBM* RNAs to all be non-dynamic regardless of PTB binding. *In vitro*, the non-dynamic RNA is indispensable for the maintenance of the condensate as RNase treatment causes both protein and RNA to dissolve, but RNA–RNA interactions are partially sufficient to maintain the *in vitro* condensates after the degradation of PTBP3 protein.

Finally, it is both the strength and number of interactions with the solid or gel-like RNA that tune protein dynamics. In oocytes, a single PTBP3 RRM–RNA interaction is sufficient to drive the localization of PTBP3 into L-bodies, but multivalent interactions between multiple RRMs and the RNA work in combination to regulate the dynamics of the protein after localization *in vivo*. In accordance with this idea, another direct *LE* RNA binding protein, Vera, was also found to be only moderately dynamic *in vivo,* with an immobile fraction of 47.1% (Neil et al., 2021). *In vitro*, it is the strength of the interaction between PTBP3 and the RNA component that determines both condensate morphology and PTBP3 dynamics: PTBP3–*LE* RNA condensates are non-spherical and have the lowest PTBP3 dynamics, whereas PTBP3–*XBM* RNA condensates are more spherical and have the highest PTBP3 dynamics. Whereas the precise % immobile fractions differ between the *in vitro* and *in vivo* systems, in each environment the *LE* RNA was significantly less dynamic than PTBP3.

## RBP binding to non-dynamic RNA facilitates the formation of non-spherical condensates

In addition to L-bodies, recent studies have identified other non-spherical biomolecular condensates, including TIS granules that form through the phase transition of an RBP, TIS11B, near the ER(Ma and

Mayr, 2018, reviwed in Fare et al., 2021). The existence of non-spherical condensates is somewhat counter-intuitive as the effects of surface tension drive many liquid-like condensates to be spherical in shape (reviewed in Hyman et al., 2014). However, non-dynamic RNAs may be a conserved mechanism to build non-spherical condensates that still have some liquid-like properties, such as highly dynamic proteins. Such non-spherical condensates are hypothesized to result from multiple small droplets flocculating together (Jawerth et al., 2020; Ranganathan and Shakhnovich, 2020). In this case, all of the available valencies within viscous condensates are hypothesized to be exhausted, preventing the ready coalescence into a larger spherical condensate. In the case of L-bodies, individual PTBP3-*LE* RNA clusters may be flocculating together, leading to the formation of the irregular shapes observed.

*In vitro* studies have provided insights into the mechanisms underlying the observed condensate morphologies. Here, we have shown the PTBP3 and *LE* RNA phase transition *in vitro* into non-spherical condensates. However, PTBP3 also phase transitions into more spherical condensates in the presence of RNAs without clear PTB binding sites, including the *mut PTB LE* and *XBM* RNAs, indicating that specific RNA–RBP interactions may drive the formation of the non-spherical condensates *in vitro*. In all cases, regardless of the morphology, RNA is non-dynamic *in vitro* and we hypothesize this to be owing to concentration-dependent rather than sequence-specific effects. Recent *in vitro* studies using a fusion protein of the RBD of TIS11B and the IDR of FUS (FUS-TIS) and various RNAs also produced condensates with varying morphologies (Ma et al., 2021). However, rather than observing morphological differences based on specific RNA–RBD binding as seen with PTBP3, FUS-TIS condensate morphology varied based on the ability of the RNA to form intermolecular RNA–RNA interactions. Additionally, RNAs in spherical FUS-TIS condensates were found to be dynamic via FRAP, whereas RNAs in non-spherical condensates were non-dynamic. The differences between the *in vitro* condensates may be owing to variation in the rate of aging of the condensates *in vitro* or differences in the type of protein tested – PTBP3 is well-folded and is only moderately dynamic via FRAP, whereas FUS-TIS contains a well-established IDR and is highly dynamic via FRAP. However, both studies demonstrate that a stable RNA component formed by certain RNAs can lead to failed condensate fusion events *in vitro*, driving the formation of a non-spherical condensate.

Although the functions of non-spherical biomolecular condensates remain unclear *in vivo*, these morphologies increase the surface area to volume ratio, increasing the interaction interface with the cytoplasm. In L-bodies, this may be beneficial for efficiently capturing RNPs that have not yet been incorporated into L-bodies and are diffusing in the cytoplasm. As the later translation of RNAs incorporated into L-bodies is required to pattern the embryo, a high degree of enrichment of localizing RNAs may be required to prevent misexpression of these transcripts. Furthermore, as *Xenopus* oogenesis occurs over extended timescales, the formation of a more solid- or gel-like condensate may be necessary for the long-term function of the condensate. As a growing number of biomolecular condensates in oocytes and embryos, including P granules in *Caenorhabditis elegans* (Putnam et al., 2019), germ granules, and *oskar* RNP granules in *Drosophila* (Bose et al., 2022; Niepielko et al., 2018; Trcek et al., 2020), and the Balbiani body and L-bodies in *Xenopus* (Boke et al., 2016; Neil et al., 2021) contain a solid or gel-like component, this may be a conserved feature of condensates in germ cells.

## Emergence of biomolecular condensates with non-dynamic RNAs and dynamic proteins

Biomolecular condensates exist on a continuum of biophysical states from a demixed liquid to a solid state, often with different components of the condensate displaying varying dynamics (reviewed in Alberti et al., 2019; Fare et al., 2021). Recent studies have demonstrated a growing variety of biomolecular condensates that have non-dynamic RNAs and comparatively dynamic proteins, including *Drosophila* germ granules, paraspeckles, and *Xenopus* L-bodies (Mao et al., 2011; Neil et al., 2021; Niepielko et al., 2018; Trcek et al., 2020). As each of these types of biomolecular condensates is enriched for RNAs, intermolecular RNA–RNA interactions may be particularly thermodynamically favorable owing to the high local concentration of RNA (reviewed in Van Treeck and Parker, 2018), driving the formation of the non-dynamic RNA. Both *in vivo* and *in vitro*, PTBP3 drives the localization of RNA into condensates, and therefore is necessary to achieve the locally high concentrations of RNA that can facilitate RNA–RNA interactions. The growing number of condensates with stable RNA components suggests that intermolecular RNA–RNA interactions driving the formation of a stable RNA substructure may be a common feature of many biomolecular condensates, giving broad relevance to the insights into the role of RNA binding in regulating protein dynamics in L-bodies.

In L-bodies, the strength and number of the interactions with the stable RNA determine PTBP3 protein dynamics *in vivo*. However, the role of other proteins, particularly proteins containing IDRs, in maintaining the

biophysical state of the L-body is not yet understood. Whereas *in vitro* PTBP3–RNA condensates and *in vivo* L-bodies contain non-dynamic RNA and moderately dynamic PTBP3, both *LE* RNA and PTBP3 were less dynamic *in vitro* than *in vivo*, suggesting that other factors contribute to the maintenance of the biophysical state of L-bodies *in vivo*. These differences highlight the limitations of minimal *in vitro* systems in studying the complex biology of phase separation, reinforcing the need to pair the mechanistic insights from *in vitro* studies with *in vivo* characterization. As L-bodies, like many other biomolecular condensates, are highly enriched for proteins with multiple RNA binding domains and IDRs, the relative contribution of each of these types of interactions to the dynamics of the condensate is an important outstanding question. For example, in FXR1 assemblies, RNA binding drives phase separation and IDRs of various lengths tune the dynamics of the condensate (Smith et al., 2020). Similarly, in L-bodies, IDR-containing proteins, which are more dynamic than PTBP3 (Neil et al., 2021), may function to keep the condensate in a more liquid-like state, perhaps preventing an irreversible transition to a solid-like state. Additionally, L-bodies contain helicases and post-translational modifying enzymes (Neil et al., 2021), which may function to remodel interactions *in vivo* to facilitate assembly and/or disassembly.

### Limitations of the study

As additional biomolecular condensates continue to be identified across an ever-growing diversity of cells and subcellular locations, it remains an important challenge to characterize the principles that are conserved or divergent across many classes of condensates. One hallmark of biomolecular condensates is the enrichment of RNA and multivalent RNA binding proteins, highlighting the importance of understanding how RNAs, proteins, and RNA–protein interactions contribute to both the composition and characteristics of condensates. Our results, which indicate that protein dynamics are tuned by multivalent interactions with a non-dynamic RNA, may provide a paradigm that is applicable to other classes of biomolecular condensates, with particular importance to solid- or gel-like condensates that regulate post-transcriptional gene expression in oocytes and early embryos. We anticipate that future studies will elucidate the range of principles underlying the functional contributions of such condensates to development and cellular function in health and disease.

## STAR★METHODS

Detailed methods are provided in the online version of this paper and include the following:

- KEY RESOURCES TABLE
- RESOURCE AVAILABILITY
  - Lead contact
  - Materials availability
  - Data and code availability
- EXPERIMENTAL MODEL AND SUBJECT DETAILS
- METHOD DETAILS
  - Oocyte isolation and culture
  - Cloning and mutagenesis
  - RNA transcription
  - Whole mount immunofluorescence (IF)
  - Analysis of RNA stability in vivo
  - RNA immunoprecipitation (RIP)
  - Recombinant protein expression and purification
  - In vitro phase transition
  - Condensate imaging
  - Condensate enzyme treatments
  - Turbidity assays
  - Immunoblotting
  - Fluorescence recovery after photobleaching (FRAP)
- QUANTIFICATION AND STATISTICAL ANALYSIS
  - Statistical details and analysis
  - Colocalization analysis
  - Condensate morphology analysis
  - Analysis of protein and RNA levels in condensates after enzymatic treatment
  - FRAP analysis

## SUPPLEMENTAL INFORMATION

Supplemental information can be found online at https://doi.org/10.1016/j.isci.2022.104811.

## ACKNOWLEDGMENTS

We thank Nicolas L. Fawzi, Erica N. Larschan, and Liam C. O'Connell for comments on the manuscript. Thank you to Nicolas L. Fawzi for gifting the *in vitro* protein expression plasmid and advice on recombinant protein expression and purification. This work was funded by R01GM071049 from the NIH to K.L.M.

## AUTHOR CONTRIBUTIONS

S.E.C. and K.L.M. conceptualized the study and contributed to the review and editing of the manuscript. K.L.M. carried out supervision, acquired funding, and contributed to visualization. S.E.C. completed the methodology development, investigation, formal analysis, visualization, and writing of the original draft. J.P.O. completed additional experiments for the revised manuscript and contributed to visualization and review and editing of the manuscript.

## DECLARATION OF INTERESTS

The authors declare no competing interests.

Received: January 31, 2022
Revised: May 24, 2022
Accepted: July 16, 2022
Published: August 19, 2022

## REFERENCES

Alberti, S., Gladfelter, A., and Mittag, T. (2019). Considerations and challenges in studying liquid-liquid phase separation and biomolecular condensates. Cell *176*, 419–434. https://doi.org/10.1016/j.cell.2018.12.035.

Banani, S.F., Lee, H.O., Hyman, A.A., and Rosen, M.K. (2017). Biomolecular condensates: organizers of cellular biochemistry. Nat. Rev. Mol. Cell Biol. *18*, 285–298. https://doi.org/10.1038/nrm.2017.7.

Banani, S.F., Rice, A.M., Peeples, W.B., Lin, Y., Jain, S., Parker, R., and Rosen, M.K. (2016). Compositional control of phase-separated cellular bodies. Cell *166*, 651–663. https://doi.org/10.1016/j.cell.2016.06.010.

Banerjee, P.R., Milin, A.N., Moosa, M.M., Onuchic, P.L., and Deniz, A.A. (2017). Reentrant phase transition drives dynamic substructure formation in ribonucleoprotein droplets. Angew. Chem. Int. Ed. Engl. *56*, 11354–11359. https://doi.org/10.1002/ange.201703191.

Birsoy, B., Kofron, M., Schaible, K., Wylie, C., and Heasman, J. (2006). Vg1 is an essential signaling molecule in Xenopus development. Development *133*, 15–20. https://doi.org/10.1242/dev.02144.

Boeynaems, S., Alberti, S., Fawzi, N.L., Mittag, T., Polymenidou, M., Rousseau, F., Schymkowitz, J., Shorter, J., Wolozin, B., Van Den Bosch, L., et al. (2018). Protein phase separation: a new phase in cell biology. Trends Cell Biol. *28*, 420–435. https://doi.org/10.1016/j.tcb.2018.02.004.

Boke, E., Ruer, M., Wühr, M., Coughlin, M., Lemaitre, R., Gygi, S.P., Alberti, S., Drechsel, D., Hyman, A.A., and Mitchison, T.J. (2016). Amyloid-like self-assembly of a cellular compartment. Cell *166*, 637–650. https://doi.org/10.1016/j.cell.2016.06.051.

Bose, M., Lampe, M., Mahamid, J., and Ephrussi, A. (2022). Liquid-to-solid phase transition of oskar ribonucleoprotein granules is essential for their function in Drosophila embryonic development. Cell *185*, 1308–1324.e23. https://doi.org/10.1016/j.cell.2022.02.022.

Burke, K.A., Janke, A.M., Rhine, C.L., and Fawzi, N.L. (2015). Residue-by-Residue view of in vitro FUS granules that bind the C-terminal domain of RNA polymerase II. Mol. Cell *60*, 231–241. https://doi.org/10.1016/j.molcel.2015.09.006.

Cabral, S.E., and Mowry, K.L. (2020). Organizing the oocyte: RNA localization meets phase separation. Curr. Top. Dev. Biol. *140*, 87–118. https://doi.org/10.1016/bs.ctdb.2020.02.007.

Clemson, C.M., Hutchinson, J.N., Sara, S.A., Ensminger, A.W., Fox, A.H., Chess, A., and Lawrence, J.B. (2009). An architectural role for a nuclear noncoding RNA: NEAT1 RNA Is essential for the structure of paraspeckles. Mol. Cell *33*, 717–726. https://doi.org/10.1016/j.molcel.2009.01.026.

Costes, S.V., Daelemams, D., Cho, E.J., Dobbin, Z., Pavlakis, G., and Lockett, S. (2004). Automatic and quantitative measurement of protein-protein colocalization in live cells. Biophysical Journal *86*, 3993–4003. https://doi.org/10.1529/biophysj.103.038422.

Cote, C.A., Gautreau, D., Denegre, J.M., Kress, T.L., Terry, N.A., and Mowry, K.L. (1999). A Xenopus protein related to hnRNP I has a role in cytoplasmic RNA localization. Mol. Cell *4*, 431–437. https://doi.org/10.1016/s1097-2765(00)80345-7.

Dale, L., Matthews, G., and Colman, A. (1993). Secretion and mesoderm-inducing activity of the TGF-beta-related domain of Xenopus Vg1. EMBO J. *12*, 4471–4480. https://doi.org/10.1002/j.1460-2075.1993.tb06136.x.

Fare, C.M., Villani, A., Drake, L.E., and Shorter, J. (2021). Higher-order organization of biomolecular condensates. Open Biol. *11*, 210137.

Fay, M.M., and Anderson, P.J. (2018). The role of RNA in biological phase separations. J. Mol. Biol. *430*, 4685–4701. https://doi.org/10.1016/j.jmb.2018.05.003.

Gagnon, J.A., Kreiling, J.A., Powrie, E.A., Wood, T.R., and Mowry, K.L. (2013). Directional transport Is mediated by a dynein-dependent step in an RNA localization pathway. PLoS Biol. *11*, e1001551. https://doi.org/10.1371/journal.pbio.1001551.

Gautreau, D., Cote, C.A., and Mowry, K.L. (1997). Two copies of a subelement from the Vg1 RNA localization sequence are sufficient to direct vegetal localization in Xenopus oocytes. Development *124*, 5013–5020. https://doi.org/10.1242/dev.124.24.5013.

Hu, J., Qian, H., Xue, Y., and Fu, X.-D. (2018). PTB/nPTB: master regulators of neuronal fate in mammals. Biophys. Rep. *4*, 204–214. https://doi.org/10.1007/s41048-018-0066-y.

Hyman, A.A., Weber, C.A., and Jülicher, F. (2014). Liquid-liquid phase separation in biology. Annu. Rev. Cell Dev. Biol. *30*, 39–58. https://doi.org/10.1146/annurev-cellbio-100913-013325.

Jain, A., and Vale, R.D. (2017). RNA phase transitions in repeat expansion disorders. Nature

*546*, 243–247. https://doi.org/10.1038/nature22386.

Jawerth, L., Fischer-Friedrich, E., Saha, S., Wang, J., Franzmann, T., Zhang, X., Sachweh, J., Ruer, M., Ijavi, M., Saha, S., et al. (2020). Protein condensates as aging Maxwell fluids. Science *370*, 1317–1323. https://doi.org/10.1126/science.aaw4951.

Jeschonek, S.P., and Mowry, K.L. (2018). Whole-mount immunofluorescence for visualizing endogenous protein and injected RNA in Xenopus oocytes. Cold Spring Harb. Protoc. *10*, 1–11.

Kafasla, P., Lin, H., Curry, S., and Jackson, R.J. (2011). Activation of picornaviral IRESs by PTB shows differential dependence on each PTB RNA-binding domain. RNA *17*, 1120–1131. https://doi.org/10.1261/rna.2549411.

Krieg, P.A., and Melton, D.A. (1984). Formation of the 3′ end of histone mRNA by post-transcriptional processing. Nature *308*, 203–206. https://doi.org/10.1038/308203a0.

Laemmli, U.K. (1970). Cleavage of structural proteins during the assembly of the head of bacteriophage T4. Nature *227*, 680–685. https://doi.org/10.1038/227680a0.

Langdon, E.M., Qiu, Y., Ghanbari Niaki, A., Mclaughlin, G.A., Weidmann, C.A., Gerbich, T.M., Smith, J.A., Crutchley, J.M., Termini, C.M., Weeks, K.M., et al. (2018). mRNA structure determines specificity ofa polyQ-driven phase separation. Science *360*, 922–927. https://doi.org/10.1126/science.aar7432.

Lewis, R.A., Kress, T.L., Cote, C.A., Gautreau, D., Rokop, M.E., and Mowry, K.L. (2004). Conserved and clustered RNA recognition sequences are a critical feature of signals directing RNA localization in Xenopus oocytes. Mech. Dev. *121*, 101–109. https://doi.org/10.1016/j.mod.2003.09.009.

Lewis, R.A., Gagnon, J.A., and Mowry, K.L. (2008). PTB/hnRNP I Is required for RNP remodeling during RNA localization in Xenopus oocytes. Mol. Cell Biol. *28*, 678–686. https://doi.org/10.1128/mcb.00999-07.

Li, P., Banjade, S., Cheng, H.C., Kim, S., Chen, B., Guo, L., Llaguno, M., Hollingsworth, J.V., King, D.S., Banani, S.F., et al. (2012). Phase transitions in the assembly of multivalent signalling proteins. Nature *483*, 336–340. https://doi.org/10.1038/nature10879.

Lin, Y., Protter, D.S.W., Rosen, M.K., and Parker, R. (2015). Formation and maturation of phase-separated liquid droplets by RNA-binding proteins. Mol. Cell *60*, 208–219. https://doi.org/10.1016/j.molcel.2015.08.018.

Livak, K.J., and Schmittgen, T.D. (2001). Analysis of relative gene expression data using real-time quantitative PCR and the 2-ΔΔCT method. Methods *25*, 402–408. https://doi.org/10.1006/meth.2001.1262.

Ma, W., and Mayr, C. (2018). A membraneless organelle associated with the endoplasmic reticulum enables 3′UTR-mediated protein-protein interactions. Cell *175*, 1492–1506.e19. https://doi.org/10.1016/j.cell.2018.10.007.

Ma, W., Zheng, G., Xie, W., and Mayr, C. (2021). In vivo reconstitution finds multivalent RNA–RNA interactions as drivers of mesh-like condensates. Elife *10*. https://doi.org/10.7554/elife.64252.

Maharana, S., Wang, J., Papadopoulos, D.K., Richter, D., Pozniakovsky, A., Poser, I., Bickle, M., Rizk, S., Guillén-boixet, J., Franzmann, T.M., et al. (2018). RNA buffers the phase separation behavior of prion-like RNA binding proteins. Science *360*, 918–921. https://doi.org/10.1126/science.aar7366.

Mao, Y.S., Sunwoo, H., Zhang, B., and Spector, D.L. (2011). Direct visualization of the co-transcriptional assembly of a nuclear body by noncoding RNAs. Nat. Cell Biol. *13*, 95–101. https://doi.org/10.1038/ncb2140.

Messitt, T.J., Gagnon, J.A., Kreiling, J.A., Pratt, C.A., Yoon, Y.J., and Mowry, K.L. (2008). Multiple kinesin motors coordinate cytoplasmic RNA transport on a subpopulation of microtubules in Xenopus oocytes. Dev. Cell *15*, 426–436. https://doi.org/10.1016/j.devcel.2008.06.014.

Mittag, T., and Parker, R. (2018). Multiple modes of protein–protein interactions promote RNP granule assembly. J. Mol. Biol. *430*, 4636–4649. https://doi.org/10.1016/j.jmb.2018.08.005.

Molliex, A., Temirov, J., Lee, J., Coughlin, M., Kanagaraj, A.P., Kim, H.J., Mittag, T., and Taylor, J.P. (2015). Phase separation by low complexity domains promotes stress granule assembly and drives pathological fibrillization. Cell *163*, 123–133. https://doi.org/10.1016/j.cell.2015.09.015.

Neil, C.R., Jeschonek, S.P., Cabral, S.E., O'Connell, L.C., Powrie, E.A., Otis, J.P., Wood, T.R., and Mowry, K.L. (2021). L-bodies are RNA–protein condensates driving RNA localization in Xenopus oocytes. Mol. Biol. Cell *32*, 1–14. https://doi.org/10.1091/mbc.e21-03-0146-t.

Niepielko, M.G., Eagle, W.V.I., and Gavis, E.R. (2018). Stochastic seeding coupled with mRNA self-recruitment generates heterogeneous Drosophila germ granules. Curr. Biol. *28*, 1872–1881.e3. https://doi.org/10.1016/j.cub.2018.04.037.

Oberstrass, F.C., Auweter, S.D., Erat, M., Hargous, Y., Henning, A., Wenter, P., Reymond, L., Amir-Ahmady, B., Pitsch, S., Black, D.L., and Allain, F.H.T. (2005). Structure of PTB bound to RNA: specific binding and implications for splicing regulation. Science *309*, 2054–2057. https://doi.org/10.1126/science.1114066.

Patel, A., Lee, H.O., Jawerth, L., Maharana, S., Jahnel, M., Hein, M.Y., Stoynov, S., Mahamid, J., Saha, S., Franzmann, T.M., et al. (2015). A liquid-to-solid phase transition of the ALS protein FUS accelerated by disease mutation. Cell *162*, 1066–1077. https://doi.org/10.1016/j.cell.2015.07.047.

Peti, W., and Page, R. (2007). Strategies to maximize heterologous protein expression in Escherichia coli with minimal cost. Protein Expr. Purif. *51*, 1–10. https://doi.org/10.1016/j.pep.2006.06.024.

Powrie, E.A., Ciocanel, V., Kreiling, J.A., Gagnon, J.A., Sandstede, B., and Mowry, K.L. (2016). Using in vivo imaging to measure RNA mobility in Xenopus laevis oocytes. Methods *98*, 60–65. https://doi.org/10.1016/j.ymeth.2015.11.003.

Putnam, A., Cassani, M., Smith, J., and Seydoux, G. (2019). A gel phase promotes condensation of liquid P granules in Caenorhabditis elegans embryos. Nat. Struct. Mol. Biol. *26*, 220–226. https://doi.org/10.1038/s41594-019-0193-2.

Ranganathan, S., and Shakhnovich, E.I. (2020). Dynamic metastable long-living droplets formed by sticker-spacer proteins. Elife *9*, 1–25. https://doi.org/10.7554/elife.56159.

Sanulli, S., and Narlikar, G.J. (2021). Generation and biochemical characterization of phase-separated droplets formed by nucleic acid binding proteins: using HP1 as a model system. Curr. Protoc. *1*, 1–18. https://doi.org/10.1002/cpz1.109.

Sawicka, K., Bushell, M., Spriggs, K.A., and Willis, A.E. (2008). Polypyrimidine-tract-binding protein: a multifunctional RNA-binding protein. Biochem. Soc. Trans. *36*, 641–647. https://doi.org/10.1042/bst0360641.

Smith, J.A., Curry, E.G., Blue, R.E., Roden, C., Dundon, S.E.R., Rodríguez-Vargas, A., Jordan, D.C., Chen, X., Lyons, S.M., Crutchley, J., et al. (2020). FXR1 splicing is important for muscle development and biomolecular condensates in muscle cells. J. Cell Biol. *219*. https://doi.org/10.1083/jcb.201911129.

Thomsen, G.H., and Melton, D.A. (1993). Processed Vg1 protein is an axial mesoderm inducer in Xenopus. Cell *74*, 433–441. https://doi.org/10.1016/0092-8674(93)80045-g.

Trcek, T., Douglas, T.E., Grosch, M., Yin, Y., Eagle, W.V.I., Gavis, E.R., Shroff, H., Rothenberg, E., and Lehmann, R. (2020). Sequence-independent self-assembly of germ granule mRNAs into homotypic clusters. Mol. Cell *78*, 941–950.e12. https://doi.org/10.1016/j.molcel.2020.05.008.

Van Treeck, B., and Parker, R. (2018). Emerging roles for intermolecular RNA-RNA interactions in RNP assemblies. Cell *174*, 791–802. https://doi.org/10.1016/j.cell.2018.07.023.

Van Treeck, B., Protter, D.S.W., Matheny, T., Khong, A., Link, C.D., and Parker, R. (2018). RNA self-assembly contributes to stress granule formation and defining the stress granule transcriptome. Proc. Natl. Acad. Sci. USA *115*, 2734–2739. https://doi.org/10.1073/pnas.1800038115.

Xie, J., Lee, J.A., Kress, T.L., Mowry, K.L., and Black, D.L. (2003). Protein kinase A phosphorylation modulates transport of the polypyrimidine tract-binding protein. Proc. Natl. Acad. Sci. USA *100*, 8776–8781. https://doi.org/10.1073/pnas.1432696100.

Yamamoto, H., Tsukahara, K., Kanaoka, Y., Jinno, S., and Okayama, H. (1999). Isolation of a mammalian homologue of a fission yeast differentiation regulator. Mol. Cell Biol. *19*, 3829–3841. https://doi.org/10.1128/mcb.19.5.3829.

## STAR★METHODS

### KEY RESOURCES TABLE

| REAGENT or RESOURCE | SOURCE | IDENTIFIER |
|---|---|---|
| Antibodies | | |
| Anti-alpha tubulin antibody | Abcam | Cat#ab4074, RRID: AB_2288001 |
| Anti-mCherry antibody | Abcam | Cat#ab62341, RRID: AB_945213 |
| Anti-RFP antibody | Abcam | Cat#ab62341, RRID: AB_945213 |
| Goat anti-rabbit IgG-HRP | Abcam | Cat#ab97200, RRID: AB_10679899 |
| Goat anti-rabbit AF647 conjugated secondary | ThermoFisher Scientific | Cat#21244, RRID: AB_2535812 |
| Normal rabbit IgG | Millipore Sigma | Cat#NI01, RRID: AB_490574 |
| Bacterial and virus strains | | |
| BL21(DE3) *E. coli* | New England Biolabs | Cat#C2527H |
| Chemicals, peptides, and recombinant proteins | | |
| Alexa Fluor 488-5-UTP | ThermoFisher Scientific | Cat#C11403 |
| Alexa Fluor 647 NHS ester | Thermo Fisher Scientific | Cat#A37573 |
| Amicon ultra 0.5 centrifugal filter unit | Millipore Sigma | Cat#UFC505024 |
| AnykD criterion TGX stain-free protein gels | Bio-Rad | Cat#5678125 |
| BL21(DE3) competent *E. coli* | New England Biolabs | Cat#C2527H |
| Black 384-well glass bottom plate | MatTek Corporation | PBK384G-1.5-C |
| ChromaTide alexa fluor 488-5-UTP | ThermoFisher Scientific | Cat#C11403 |
| Ciprofloxacin | Millipore Sigma | Cat#17850 |
| Collagenase from *Clostridium histolyticum* | Millipore Sigma | Cat#C0130 |
| Coomassie brilliant blue R-250 dye | ThermoFisher Scientific | Cat#20278 |
| Cytiva amersham CyDye fluorescent nucleotides, Cy3-UTP | Fisher Scientific | Cat# PA55026 |
| Cytiva amersham CyDye fluorescent nucleotides, Cy5-UTP | Fisher Scientific | Cat#PA55026 |
| Formaldehyde, 37%, microfiltered | Electron Microscopy Science | Cat#15686 |
| Illustra ProbeQuant G-50 micro columns | Millipore Sigma | Cat#28-9034-08 |
| Gentamicin | ThermoFisher Scientific | Cat#15750060 |
| Gibson assembly master mix | New England Biolabs | Cat#E2611L |
| Halt protease inhibitor cocktail, EDTA-free (100X) | ThermoFisher Scientific | Cat#78439 |
| Invitrogen RNase cocktail enzyme mix | ThermoFisher Scientific | Cat#AM2286 |
| IPTG | Millipore Sigma | Cat#I6758 |
| Leibovitz's L-15 medium | ThermoFisher Scientific | Cat#11415064 |
| Ni-NTA agarose | Qiagen | Cat#30210 |
| Nystatin | Millipore Sigma | Cat#N1638 |
| Penicillin streptomycin | ThermoFisher Scientific | Cat#15140122 |
| Phusion high-fidelity PCR master mix | New England Biolabs | Cat#M051S |
| Pierce IgG elution buffer | ThermoFisher Scientific | Cat#21028 |
| Pierce protein A/G magnetic beads | ThermoFisher Scientific | Cat#88803 |
| PowerUp SybrGreen Master Mix | ThermoFisher Scientific | Cat#A25742 |
| Precision plus protein kaliedoscope protein standards | Bio-Rad | Cat#1610375 |

(*Continued on next page*)

*Continued*

| REAGENT or RESOURCE | SOURCE | IDENTIFIER |
|---|---|---|
| Proteinase K from *Tritachium album* | Millipore Sigma | Cat#P2308 |
| Ribolock RNAse inhibitor | ThermoFisher Scientific | Cat#EO0381 |
| SecureSeal imaging spacers | Grace Bio-labs | Cat#470352 |
| ssRNA ladder | New England Biolabs | Cat#N0362S |
| Super-Signal west pico plus chemiluminescent substrate | ThermoFisher Scientific | Cat#34580 |
| ThermalSeal | Excel Scientific | TS-RT2-100 |
| Turbo DNase | ThermoFisher Scientific | Cat#AM2238 |
| **Critical commercial assays** | | |
| iScript cDNA synthesis kit | Bio-Rad | Cat#1708891 |
| MEGAclear transcription clean-up kit | ThermoFisher Scientific | Cat#AM1908 |
| MEGAscript T7 transcription kit | ThermoFisher Scientific | Cat#AM1334 |
| mMESSAGE mMACHINE SP6 transcription kit | ThermoFisher Scientific | Cat#AM1340 |
| Qubit RNA broad range assay kit | ThermoFisher Scientific | Cat#Q1021 |
| RNeasy Plus Micro Kit | Qiagen | Cat#74034 |
| **Experimental models: Organisms/strains** | | |
| *Xenopus laevis*, Nasco background, female | Nasco | Cat#LM00535MX |
| **Oligonucleotides** | | |
| Barcode A *vg1 LE* forward | Neil et al. (2021) | PCR primer |
| Barcode B *vg1 LE* forward | Neil et al. (2021) | PCR primer |
| Barcode C *XBM* forward | Neil et al. (2021) | PCR primer |
| *vg1 LE* reverse | Neil et al. (2021) | PCR primer |
| *XBM* reverse | Neil et al. (2021) | PCR primer |
| Barcode A qPCR forward | Neil et al. (2021) | qPCR primer |
| Barcode B qPCR forward | Neil et al. (2021) | qPCR primer |
| Barcode C qPCR forward | Neil et al. (2021) | qPCR primer |
| *GAPDH* qPCR forward | Neil et al. (2021) | qPCR primer |
| *GAPDH* qPCR reverse | Neil et al. (2021) | qPCR primer |
| *LE* qPCR reverse | Neil et al. (2021) | qPCR primer |
| *luciferase* qPCR forward | Neil et al. (2021) | qPCR primer |
| *luciferase* qPCR reverse | Neil et al. (2021) | qPCR primer |
| *vg1* qPCR forward | Neil et al. (2021) | qPCR primer |
| *XBM* qPCR reverse | Neil et al. (2021) | qPCR primer |
| Luciferase control RNA | Promega | Cat#L4561 |
| **Recombinant DNA** | | |
| pET:THMT | Peti and Page (2007) | N/A |
| pET:THMT:PTBP3 | This study | N/A |
| pSP64TSNRLMCS:mCherry | Neil et al. (2021) | N/A |
| pSP64TSNRLMCS:mCh-PTBP1 | This study | N/A |
| pSP64TSNRLMCS:mCh-PTBP3 | This study | N/A |
| pSP64TSNRLMCS:mCh-PTBP3 mut12 | This study | N/A |
| pSP64TSNRLMCS:mCh-PTBP3 mut1234 | This study | N/A |
| pSP64TSNRLMCS:mCh-PTBP3 mut3 | This study | N/A |
| pSP64TSNRLMCS:mCh-PTBP3 mut34 | This study | N/A |
| pSP64TSNRLMCS:mCh-PTBP3 mut4 | This study | N/A |

(*Continued on next page*)

*Continued*

| REAGENT or RESOURCE | SOURCE | IDENTIFIER |
|---|---|---|
| pSP64TSNRLMCS:Vera-mCh | Neil et al. (2021) | N/A |
| pSP64TSNRLMCS:XBM5 | Krieg and Melton (1984) | N/A |
| pSP73:2X135 | Gautreau et al. (1997) | N/A |
| pSP73:2X135 ΔVM1 | Lewis et al. (2004) | N/A |
| Software and algorithms | | |
| ImageJ | NIH | https://imagej.nih.gov/ij/ |
| Analyze particle ImageJ plugin | N/A | https://imagej.nih.gov/ij/docs/menus/analyze.html |
| Colocalization threshold ImageJ plugin | Costes et al., 2004 | https://imagej.net/plugins/colocalization-threshold |
| Time series analyzer V3 ImageJ plugin | N/A | https://imagej.nih.gov/ij/plugins/time-series.html |
| Prism 9 | GraphPad | https://www.graphpad.com/scientific-software/prism/ |
| Other | | |
| Illustra ProbeQuant G50 micro column | GE Healthcare | Cat#28-9034-08 |
| PTBP3 gBlock gene fragment | Integrated DNA Technologies | PTBP3 gBlock |

## RESOURCE AVAILABILITY

### Lead contact

Further information and requests for resources and reagents should be directed to and will be fulfilled by the Lead Contact, Kimberly Mowry (kimberly_mowry@brown.edu).

### Materials availability

This study did not generate new unique reagents. Plasmids generated in this study are available from the lead contact upon completion of an MTA.

### Data and code availability

- Data reported in this paper will be shared by the lead contact upon request.
- This paper does not report original code.
- Any additional information required to reanalyze the data reported in this paper is available from the lead contact upon request.

## EXPERIMENTAL MODEL AND SUBJECT DETAILS

Oocytes used in this study were surgically harvested from wild-type *Xenopus laevis* females (Nasco). All animal experiments were approved by the Brown University Institutional Animal Care and Use Committee.

## METHOD DETAILS

### Oocyte isolation and culture

Oocytes were defolliculated using 2 mg/mL collagenase (Sigma), and washed in MBSH [88 mM NaCl, 1 mM KCl, 2.4 mM $NaHCO_3$, 0.82 mM $MgSO_4$, 0.33 mM $Ca(NO_3)_2$, 0.41 mM $CaCl_2$, 100mM HEPES (pH 7.6)]. Stage II-III oocytes were manually sorted, and cultured at 18°C in OCM+ [50% Leibovitz L-15 medium, 15 mM HEPES (pH 7.6), 1 mg/mL insulin, 50 U/mL nystatin (Sigma), 100 U/mL penicillin/streptomycin (ThermoFisher), 0.1 mg/mL gentamicin (ThermoFisher), 0.1 mg/mL ciprofloxacin] (Sigma).

### Cloning and mutagenesis

RNA from stage II-III oocytes was isolated by Trizol extraction and reverse transcribed into cDNA using iScript cDNA synthesis kit. PTBP3 specific primers (Table S2) were used to amplify PTBP3 cDNA using Phusion

high fidelity master mix and cloned in the pSP64TSNRLMCS:mCherry (Neil et al., 2021) and pET:THMT (Peti and Page, 2007) vectors. A gBlock gene fragment for the PTBP3 quadruple mutant (IDT) was cloned into pSP64TSNRLMCS:mCherry vector using Gibson Assembly master mix (New England Biolabs). Single and double mutants were created by ligating portions of the WT and quadruple mutant gene together using Gibson Assembly Master Mix and cloning into the pSP64TSNRLMCS:mCherry vector.

### RNA transcription

For protein coding RNAs, RNAs were transcribed *in vitro* with the mMessage machine SP6 kit (ThermoFisher) using the following linearized plasmids as the DNA template: pSP64TSNRLMCS:mCh-PTBP3, pSP64TSNRLMCS:mCh-PTBP3 mut12, pSP64TSNRLMCS:mCh-PTBP3 mut34, pSP64TSNRLMCS:mCh-PTBP3 mut3, pSP64TSNRLMCS:mCh-PTBP3 mut4, pSP64TSNRLMCS:mCh-PTBP3 mut1234, pSP64TSNRLMCS:mCh, pSP64:mCh-PTBP1, and pSP64TSNRLMCS:Vera-mCh (Neil et al., 2021). RNAs were extracted with phenol/chloform/isoamyl alcohol (25:24:1; ThermoFisher) and precipitated with 1 volume of isopropanol as in (Jeschonek and Mowry, 2018). The concentration of the RNA was measured via Qubit RNA broad range assay (ThermoFisher).

For the barcoded RNAs, RNAs were transcribed *in vitro* with the MEGAscript T7 kit (ThermoFisher) using length matched PCR products as the DNA templates. PCR products were generated from the following plasmids, with the forward primer for each construct containing the T7 promoter sequence and the unique barcode sequence as shown in Table S2: pSP73:2x135 (*LE*) (Gautreau et al., 1997), pSP73:2 × 135ΔVM1 (*mut PTB LE*) (Lewis et al., 2004), pSP64:XBM (*XBM*) (Krieg and Melton, 1984). To synthesize fluorescently labelled RNAs for oocyte microinjection, RNAs were transcribed as above in the presence of 250 nM Cy3- or Cy5-UTP (ThermoFisher). For fluorescently labelled RNAs for *in vitro* experiments, RNAs were transcribed as above in the presence of 500 nM Alexa Fluor 488-UTP (ThermoFisher). T7 transcribed RNAs were cleaned up using MEGAclear transcription clean up kits (ThermoFisher) and the concentration of RNA was measured via Qubit RNA broad range assay (ThermoFisher).

### Whole mount immunofluorescence (IF)

Oocytes were microinjected with 2 nL of 500 nM RNA encoding an mCh-PTBP3 construct and 250 nM Cy5-UTP labelled *LE* RNA to mark L-bodies. Oocytes were cultured for 48 h in OCM+, fixed for 1 h in fixation buffer [80 mM PIPES (pH 6.8), 1 mM $MgCl_2$, 5 mM EGTA, 0.2% Triton X-100, 3.8% formaldehyde], and washed 3 times for 15 min. each in PBT [137 mM NaCl, 2.7 mM KCl, 10 mM $Na_2HPO_4$, 1.8 mM $KH_2PO_4$, 0.2% BSA, 0.1% Triton X-100]. Oocytes were blocked for 4 h at room temperature in PBT+ [PBT supplemented with 2% goat serum and 2% BSA], incubated overnight at 4°C in a 1:500 dilution of anti-mCh primary antibody (Abcam) in PBT+, and washed 3 times for 2 h each in PBT. Oocytes were incubated overnight at 4°C in a 1:1000 dilution of goat, anti-rabbit AF647 conjugated secondary antibody (ThermoFisher), washed 3 times for 2 h each, dehydrated in anhydrous methanol, and frozen at −20°C until imaging. Immediately prior to imaging, oocytes were cleared in BABB solution (1:2 benzyl alcohol:benzyl benzoate). Oocytes were imaged on an inverted Olympus FV3000 confocal microscope using 20× UPlan Super Apochromat objective (air, NA = 0.75) and 60× UPlan Super Apochromat objective (silicon oil, NA = 1.3) using GaAsP detectors.

### Analysis of RNA stability in vivo

Stage II oocytes were microinjected with 250 nM barcoded *LE* RNA and *LE* RNA levels were measured at 0-, 24-, and 48-h post-injection by RT-qPCR. Analysis was completed using the delta delta $C_T$ method (Livak and Schmittgen, 2001), normalizing to 0 h, and using GAPDH as a control.

### RNA immunoprecipitation (RIP)

For the endogenous RIPs, approximately 600 stage II-III oocytes per protein condition were microinjected with 2 nL of 500 nM Vera-mCh, mCh-PTBP3 WT, or mCh-PTBP3 mut1234 RNA. Oocytes were cultured for 48 h at 18°C in OCM+. Oocytes were then crosslinked with 0.1% formaldehyde in PBS for 10 min. at room temperature and then quenched for 5 min. in 250 mM glycine in 25 mM Tris (pH 7.4). Oocytes were then lysed in RIP buffer and clarified twice by centrifugation at 10,000×*g* for 10 min. at 4°C. 5 mg of antibody [anti- mCh (Abcam) or Normal rabbit IgG (Sigma] was added to each reaction and incubated for 1 h at 4°C with rotation. Next, 15 µL of Pierce Protein A/G magnetic beads in RIP buffer were added to each reaction and incubated for an additional 4 h at 4°C, the beads were washed 3 times in RIP buffer, and bound

proteins and RNAs were eluted from the beads in Pierce IgG Elution Buffer (ThermoFisher) via shaking (1200 rpm) at 24°C for 20 min. After removal of the eluent from the beads, crosslinking was reversed by incubation at 70°C for 45 min. To control for RNA extraction efficiency, 2.5 pg of luciferase control RNA (Promega) was added to each sample prior to RNA extraction using RNeasy Plus Micro Kit (Qiagen). cDNA synthesis was performed using iScript cDNA synthesis kit (Biorad), and qRT-PCR was performed for *luciferase* and *vg1* RNAs using PowerUp SybrGreen Master Mix (ThermoFisher) per the manufacturer's protocol using primers shown in Table S3.

For the barcoded RNA RIPs, 600 stage II-III oocytes per protein expressed were microinjected with 2 nL of 500 nM mCh-PTBP3 WT or mCh-PTBP3 mut1234 RNA and 150 nM *Barcode A- vg1 LE*, 150 nM *Barcode B- mut PTB LE*, and 150 nM *Barcode C- XBM* RNAs. Oocytes were cultured and RIPs were performed as described above without crosslinking and decrosslinking of the samples. qRT-PCR was performed for *luciferase*, *Barcode A*, *Barcode B*, and *Barcode C* using primers shown in Table S3.

For the combinatorial PTBP3 RRM mutant RIPs, 200 stage II-III oocytes per protein expressed condition were microinjected with 2 nL of 500 nM mCh-PTBP3 WT, mCh-PTBP3 mut12, mCh-PTBP3 mut34, mCh-PTBP3 mut 3, mCh-PTBP3 mut 4, or mCh-PTBP3 mut1234 RNA and 150 nM *Barcode A- vg1 LE*. Oocytes were cultured and RIPs were completed as described above without crosslinking and decrosslinking of the samples. qRT-PCR was performed for *luciferase* and *Barcode A* using primers shown in Table S3.

### Recombinant protein expression and purification

MBP-PTBP3 fusion protein was expressed in BL21(DE3) *E. coli* (New England Biolabs) transformed with pET:THMT:PTBP3 at 15°C overnight with 400 μM IPTG (Sigma). Induced pellets were resuspended in low imidazole purification buffer [20 mM sodium phosphate (pH 7.4), 1 M NaCl, 10 mM imidazole, and 1× Halt protease inhibitors (ThermoFisher)] and lysed via sonication. The suspension was cleared by centrifugation at 28,960 RCF for 30 min. at 4°C, and the resulting supernatant was bound to Ni-NTA agarose (Qiagen) for 1 h at 4°C, washed in 5 bed volumes of low imidazole purification buffer, and eluted in high imidazole purification buffer [20 mM sodium phosphate (pH 7.4), 1 M NaCl, 300 mM imidazole, and 1× Halt protease inhibitor cocktail (ThermoFisher)]. Fractions containing MBP-PTBP3 were pooled, concentrated, buffer exchanged into storage buffer [20 mM sodium phosphate (pH 7.4), 250 mM NaCl], and flash frozen. A260/280 ratios were taken using a Nanodrop One to measure nucleic acid contamination.

### In vitro phase transition

Purified MBP-PTBP3 protein was incubated with TEV protease for 2 h at room temperature to cleave off the MBP (maltose binding protein) tag. Protein for fluorescent imaging was labelled with AF647-NHS Ester (ThermoFisher) by resuspending the AF-647 in DMSO and incubating with cleaved PTBP3 protein for 1 h at room temperature. Excess AF-647 was removed in a G50 micro column (GE Healthcare). Labelled protein was buffer exchanged into 2× PTBP3 phase buffer [100 mM Tris (pH 7.5), 200 mM NaCl, 2 mM DTT]. Cleaved PTBP3 protein was diluted to 25 μM in 2× PTBP3 phase buffer with 10% fluorescent labelling for microscopy assays. 30 ng/μL stocks of *in vitro* transcribed RNA with 25% Alexa Fluor 488-UTP labelled RNA in DEPC-treated $H_2O$ for microscopy assays were denatured at 72°C for 10 min. and stored on ice. In a 20 μL reaction, 10 μL of PTBP3 protein (12.5 μM final protein concentration) and 10 μL of RNA (15 ng/μL final RNA concentration) were mixed and incubated for 1 h at room temperature.

### Condensate imaging

Condensates were imaged by placing 15 μL of the phase transition reaction onto a #1.5 coverslip with imaging spacers (Grace Bio-labs) and sealed with a slide (total imaging depth of ~0.24 mM). Condensates were imaged on an inverted Olympus FV3000 confocal microscope using a 60× UPlan Super Apochromat objective (silicon oil, NA = 1.3) and 5× digital zoom.

### Condensate enzyme treatments

20 μL of the PTBP3-RNA condensates were prepared as described above and then pipetted onto a #1.5 coverslip. Samples were then treated with 2 μL of TURBO DNase (Invitrogen), 2 μL of RNase Cocktail (Invitrogen), or 2 μL of 12.5 μg/μL Proteinase K (Sigma, 12.5 mg/mL) and live imaged every 5 s for 75 cycles on an inverted Olympus FV3000 confocal microscope using a 60× UPlan Super Apochromat objective (silicon oil, NA = 1.3) and 5× digital zoom.

### Turbidity assays

For the NaCl concentration series, *in vitro* reactions were prepared as described above in 50 mM Tris (pH 7.5), 1 mM DTT, and the indicated NaCl concentration (25, 100, 250, 500 mM, or 1 M). 12.5 μM PTBP3 was incubated with 0 ng/μL RNA (PTBP3 alone) or 15 ng/μL *LE* RNA (PTBP3 & *vg1 LE*). For the RNA concentration series, *in vitro* reactions were prepared as described above in 50 mM Tris (pH 7.5), 100 mM NaCl, 1 mM DTT. 12.5 μM PTBP3 (PTBP3 & *LE*) or buffer controls (*LE* alone,) were incubated with the indicated RNA concentration of *LE* RNA (0 ng/μL, 15 ng/μL, 37.5 ng/μL, and 75 ng/μL). Turbidity was assayed in a 384-well glass bottom plate (MatTek Corporation) with 20 μL samples sealed with clear optical film (Excel Scientific) to prevent evaporation. Absorbance of the samples at 600 nm was read using a Cytation 5 Multi-Mode Reader (BioTek) after 1 h of incubation at room temperature. Absorbance data was normalized to buffer and TEV protease controls. In the turbidity assays, no fluorescent labels were used for either the protein or RNA.

### Immunoblotting

25 oocytes per mCh-PTBP3 construct and uninjected controls were homogenized in 50 μL of RIP buffer [25 mM Tris (pH 7.4), 0.5% NP40, 0.5 mM DTT, 150 mM KCl, 5 mM EDTA, 10 mM $C_4H_6MgO_4$, 1× Halt protease inhibitors (ThermoFisher), and 2 nU/mL Ribolock RNase inhibitor (ThermoFisher)]. Lysates were clarified via centrifugation at 10,000×*g* for 10 min. at 4°C and then boiled in Laemmli sample buffer (Laemmli, 1970). For immunoblotting, anti-mCh (Abcam) and anti-tubulin (Abcam) primary antibodies were used at 1:1000. Secondary goat anti-rabbit IgG-HRP antibody (Abcam) was used at 1:15,000. Blots were developed using SuperSignal West Pico PLUS chemiluminescent substrate (ThermoFisher) and imaged using a Bio-Rad ChemiDoc.

### Fluorescence recovery after photobleaching (FRAP)

For the oocyte FRAP, Stage II oocytes were microinjected with 2 nL of 500 nM RNA encoding mCh-PTBP3 and 250 nM Cy5-UTP labelled *LE* RNA for FRAP of PTBP3 wild-type and mutant proteins. For RNA FRAP, 2 nL of 250 nM Cy3-UTP labelled test RNA (*LE, mut PTB LE,* or *XBM*) was microinjected into stage II oocytes, along with 250 nM Cy5-UTP labelled *LE* RNA to mark the L-bodies. Microinjected oocytes were cultured for 48 h in OCM+. Seven oocytes per biological replicate (n = 21 oocytes total per construct tested) were analyzed. A 10 $\mu m^2$ ROI was bleached using the 488 nm laser at 100% for 2 s. Fluorescence recovery was monitored every 5 s for 100 iterations.

For the *in vitro* condensate FRAP, 7 condensates per replicate (n = 21 condensates total per RNA) were analyzed. For whole condensate FRAP, a 2 $\mu m^2$ ROI was bleached using the 405 nm laser at 50% and the 561 nm laser at 100% for 0.8 s. For partial condensate FRAP, a 1 $\mu m^2$ ROI was bleached using the 405 nm laser at 50% and the 561 nm laser at 100% for 0.4 s. Fluorescence recovery was monitored every 5 s for 50 iterations.

## QUANTIFICATION AND STATISTICAL ANALYSIS

### Statistical details and analysis

Statistical details of experiments, including exact value of n, what n represents, definition of center and dispersion, and the statistical tests used are detailed in the figure legends. Significance was defined according to the following: ns indicates $p > 0.5$, * indicates $0.1 < p < 0.5$, ** indicates $0.01 < p < 0.1$, *** indicated $0.01 < p < 0.001$, and **** indicates $p < 0.001$.

### Colocalization analysis

For each of the mCh-PTBP3 wild-type and mutant constructs, images of 10 oocytes in each of 3 biological replicates (n = 30 oocytes) were collected for analysis using a 20× air objective with a 1.2× digital zoom. Working from the top, left corner of the imaging dish, the first 10 oocytes for which *LE* localization was observed in the perinuclear cup, in L-bodies, and at the vegetal cortex were selected. Colocalization analysis was completed in ImageJ using the Colocalization threshold plugin using an ROI surrounding the oocyte. Statistics shown are an Ordinary one-way ANOVA with Tukey's multiple comparison correction.

### Condensate morphology analysis

Condensate morphology was analyzed on 5 fields of view per replicate (n = 15 fields of view total per RNA). Condensate number, size, and circularity were calculated based on manual thresholding of AF-647 labelled PTBP3 fluorescence using the "Analyze Particles" plugin in ImageJ. Condensates of any circularity and

greater than 5 pixels in area were analyzed, excluding all condensates on the edge of the image. Partition coefficients (MCC) were calculated from the same analysis images using the "Colocalization Threshold" plugin in ImageJ. Statistics shown are an Ordinary one-way ANOVA with Tukey's multiple comparison correction.

### Analysis of protein and RNA levels in condensates after enzymatic treatment

To analyze protein and RNA over time after treatment with DNase, RNase, and Proteinase K, 50 × 50 ROIs were placed over stationary condensates, and fluorescence was quantified using the Time Series Analyzer V3 (https://imagej.nih.gov/ij/plugins/time-series.html).

### FRAP analysis

FRAP calculations were performed as detailed (Gagnon et al., 2013; Powrie et al., 2016). First, we adjusted for photobleaching by calculating *A(t)* for the region of interest (ROI) of the time series fluorescence data with the following equation:

$$A(t) = F(t) \times \frac{F_{pre}}{F_n(t)} = (ROI(t) - ROI_o(t)) \times \frac{(ROI_n(1) - ROI_o(1))}{(ROI_n(t) - ROI_o(t))}$$

where *F(t)* is the background subtracted fluorescence at time *t*, $F_{pre}$ is the background subtracted average intensity for the prebleach frames, $F_n(t)$ is the background subtracted fluorescence intensity value of a neighboring region at the time *t*, *ROI(t)* represents the raw fluorescence data from the photobleached ROI at time *t*, $ROI_o(t)$ and $ROI_n(t)$ are fluorescence data from the non-photobleached regions outside (*o*) and inside (*n*) the oocyte at time *t*. Second, the adjusted data *A(t)* was normalized further against the pre-bleach values by calculating the normalize adjusted fluorescence time series $A_{norm}(t)$:

$$A_{norm}(t) = \frac{A_t}{F_{pre}} = \frac{A(t)}{(ROI(1) - ROI_o(1))}$$

We then further calculated the further normalized time series *N(t)*:

$$N(t) = \frac{A_{norm}(t) - A_{norm}(1)}{A_{norm,pl} - A_{norm}(1)}$$

where the photobleach corrected fluorescence intensity at the first time point after bleaching is $A_{norm}(1)$ and the average photobleach corrected fluorescence intensity at the plateau is $A_{norm,pl}$. The data was analyzed via one phase non-linear regression and two phase non-linear regression analyses using GraphPad Prism 9. Statistics shown in the main text for the percent immobile fractions are an Ordinary one-way ANOVA with Tukey's multiple comparison correction of the one phase association data. All percent immobile fraction data is summarized in Table S4.